nature immunology

ARTICLES

https://doi.org/10.1038/s41590-021-01083-0

Check for updates

Aging disrupts circadian gene regulation and function in macrophages

Eran Blacher[1,11], Connie Tsai[1,2,11], Lev Litichevskiy[3,4,5,11], Zohar Shipony[6], Chinyere Agbaegbu Iweka[1], Kai Markus Schneider[3,4,5], Bayarsaikhan Chuluun[7], H. Craig Heller[7], Vilas Menon[8], Christoph A. Thaiss[3,4,5,12] ✉ and Katrin I. Andreasson[1,9,10,12] ✉

Aging is characterized by an increased vulnerability to infection and the development of inflammatory diseases, such as atherosclerosis, frailty, cancer and neurodegeneration. Here, we find that aging is associated with the loss of diurnally rhythmic innate immune responses, including monocyte trafficking from bone marrow to blood, response to lipopolysaccharide and phagocytosis. This decline in homeostatic immune responses was associated with a striking disappearance of circadian gene transcription in aged compared to young tissue macrophages. Chromatin accessibility was significantly greater in young macrophages than in aged macrophages; however, this difference did not explain the loss of rhythmic gene transcription in aged macrophages. Rather, diurnal expression of Kruppel-like factor 4 (*Klf4*), a transcription factor (TF) well established in regulating cell differentiation and reprogramming, was selectively diminished in aged macrophages. Ablation of *Klf4* expression abolished diurnal rhythms in phagocytic activity, recapitulating the effect of aging on macrophage phagocytosis. Examination of individuals harboring genetic variants of *KLF4* revealed an association with age-dependent susceptibility to death caused by bacterial infection. Our results indicate that loss of rhythmic *Klf4* expression in aged macrophages is associated with disruption of circadian innate immune homeostasis, a mechanism that may underlie age-associated loss of protective immune responses.

Circadian rhythms are endogenous, free-running cycles with periodicities of approximately 24 h. Circadian rhythms are entrained by environmental cues and enable organisms to alter their physiology and behavior to anticipate changes in their environment[1]. In mammals, these rhythms are coordinated by the light-entrained master pacemaker in the suprachiasmatic nucleus in the hypothalamus. Within suprachiasmatic nucleus neurons, transcription–translation feedback loops involving the activator core clock protein heterodimer BMAL1/CLOCK and the repressor PER/CRY generate a circadian molecular oscillator. These TFs translocate to the nucleus, where they bind to consensus enhancer box (E-box) DNA motifs of circadian-regulated genes.

Peripheral cells similarly possess endogenous circadian clocks that are governed by the same TF feedback loop[2]. Comparisons of circadian-regulated genes across multiple organ systems indicate that almost half of all protein-coding genes can be regulated in a diurnal fashion across different tissues[3,4]. This tissue-specific circadian gene expression regulates biological processes essential for the maintenance and dynamic changes of individual organ functions over the circadian cycle.

In the immune system, the diurnal rhythmicity of immune responses ranges from leukocyte trafficking and maintenance of immunosurveillance to recognition of pathogens and engagement of defensive responses[5–8]. Within the innate immune system, major components of myeloid responses, including phagocytic capacity, release of cytokines and chemokines, cell trafficking and expression of innate immune Toll-like receptors (TLRs), are tightly regulated and follow distinct circadian phases[8–16]. The strict temporal gating of innate immune cell functions ensures the maintenance of homeostasis through an organized sequence of immune defensive responses to pathogens. Indeed, experimental disruption of immune circadian rhythmicity amplifies disease-causing inflammation and aggravates pathology in models of infection or high-fat diet[8,17,18].

Aging is associated with an increased incidence of many diseases, including cancer, cardiovascular disease, metabolic syndrome and neurodegeneration. The onset and progression of these common diseases are strongly linked to age-associated changes in immune function. Aging is also characterized by marked dysregulation of immune function, including the development of a bias toward myeloid over lymphoid cell differentiation[19], disrupted mitochondrial respiration and energy metabolism[20], increased vulnerability to viral and bacterial infections and persistent low-grade inflammation. We hypothesized that immune circadian rhythmicity might be disrupted with aging, leading to maladaptive responses that contribute to changes seen in the aging immune system.

Results

Aging abolishes diurnal innate immune responses. We examined whether diurnal features of the innate immune response were preserved in aged mice, with a particular focus on immune cell trafficking, response to lipopolysaccharide (LPS) and phagocytosis. We first investigated diurnal trafficking of Ly6C^{hi} inflammatory monocytes

[1]Department of Neurology & Neurological Sciences, Stanford School of Medicine, Stanford, CA, USA. [2]Neurosciences Graduate Program, Stanford University, Stanford, CA, USA. [3]Department of Microbiology, Perelman School of Medicine, University of Pennsylvania, Philadelphia, PA, USA. [4]Institute for Immunology, Perelman School of Medicine, University of Pennsylvania, Philadelphia, PA, USA. [5]Institute for Diabetes, Obesity, and Metabolism, Perelman School of Medicine, University of Pennsylvania, Philadelphia, PA, USA. [6]Department of Genetics, Stanford University, Stanford, CA, USA. [7]Department of Biology, Stanford University, Stanford, CA, USA. [8]Center for Translational and Computational Neuro-immunology, Department of Neurology, Columbia University Medical Center, New York, NY, USA. [9]Stanford Immunology Program, Stanford University, Stanford, CA, USA. [10]Wu Tsai Neurosciences Institute, Stanford University, Stanford, CA, USA. [11]These authors contributed equally: Eran Blacher, Connie Tsai, Lev Litichevskiy. [12]These authors jointly supervised this work: Katrin I. Andreasson, Christoph A. Thaiss. ✉e-mail: thaiss@pennmedicine.upenn.edu; kandreas@stanford.edu

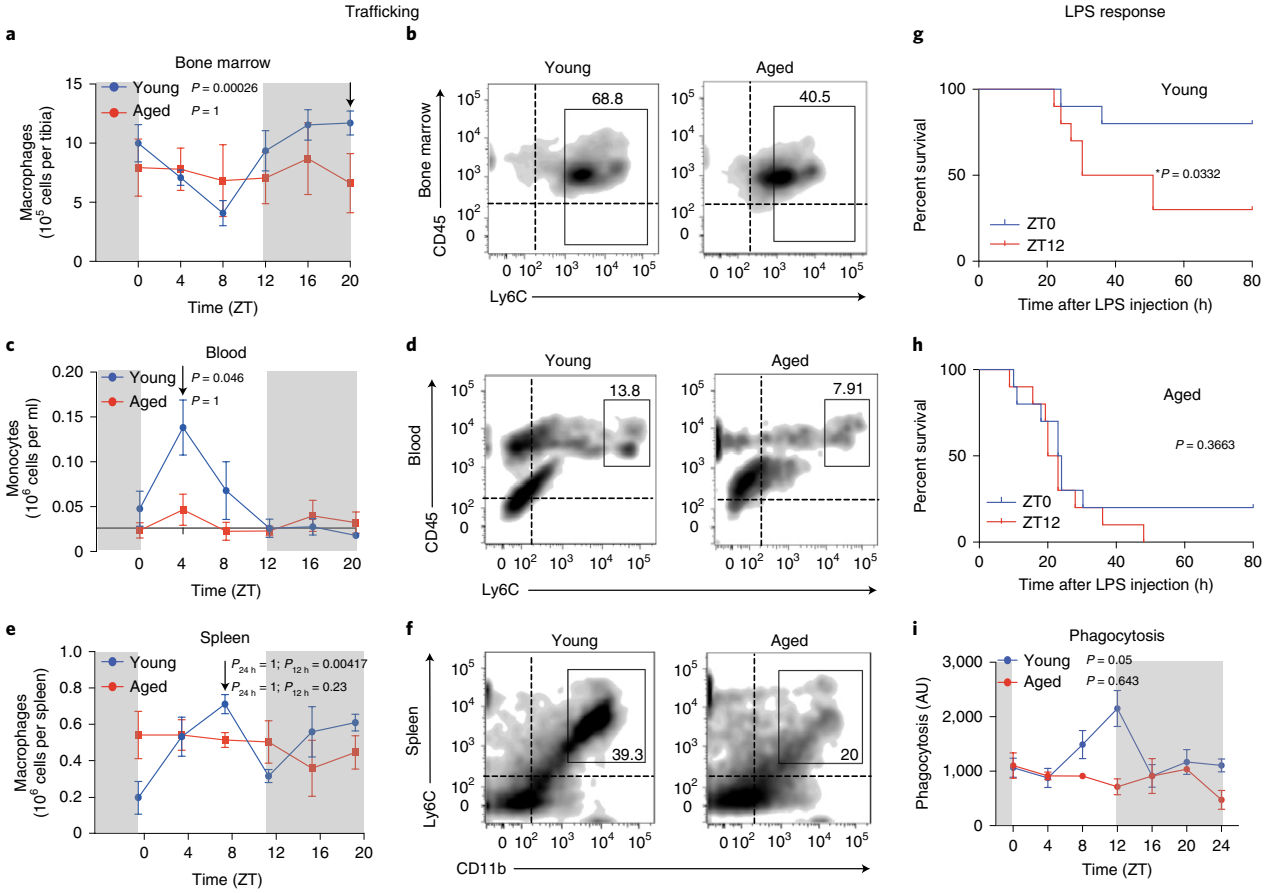

Fig. 1 | Aging disrupts the diurnal rhythmicity of innate immune functions. a–f, Young (2-month-old) and aged (20- to 22-month-old) C57B6/J male mice were examined for monocyte trafficking from the bone marrow to the blood and spleen ($n=3$ per time point per age). Samples were analyzed by flow cytometry at Zeitgeber time (ZT) 4, 8, 12, 16, 20 and 24 h. Vertical black arrows in **a**, **c** and **e** denote the maximum number of cells in the young age group featured in the representative plots **b**, **d** and **f**. The experiment was repeated twice. In **a**, **c** and **e**, data represent mean ± s.e.m. The numbers of $CD45^+CD11b^+Ly6C^+$ bone marrow macrophages in young versus aged mice ($P=0.00026$ and $P=1$ for young and aged mice, respectively, by JTK_CYCLE) were calculated (**a**,**b**) as well as the numbers of $CD45^+CD11b^+Ly6C^+$ blood monocytes in young versus aged mice ($P=0.046$ and $P=1$ for young and aged mice, respectively, by JTK_CYCLE) (**c**,**d**) and $CD45^+CD11b^+Ly6C^+$ spleen macrophages in young versus aged mice ($P=1$ for young and aged mice (24-h cycle) and $P=0.00417$ and $P=0.23$ for young and aged mice (12 h), respectively, by JTK_CYCLE) (**e**,**f**). Numbers in the top-right quadrants indicate percentage of $CD45^+CD11b^+Ly6C^+$ macrophages. **g**,**h**, Young (**g**) and aged (**h**) mice were administered 25 mg kg^{-1} LPS at ZT0 (blue line, 'lights on') or ZT12 (red line, 'lights off') and monitored for 7 d; $n=10$ mice in each group; $^*P<0.05$, log-rank test. **i**, Young and aged peritoneal macrophages were assayed for phagocytosis of fluorescent *Escherichia coli* particles over a 24-h period; $P=0.05$ and $P=0.643$ for young and aged mice, respectively, by JTK_CYCLE ($n=3$ mice per time point per age). The experiment was repeated twice. Data represent mean ± s.e.m; AU, arbitrary units.

from the bone marrow to the blood, a homeostatic myeloid process critical to antimicrobial immune defense[8]. Blood monocytes, bone marrow macrophages and spleen macrophages were isolated from young (2- to 3-month-old) and aged (18- to 20-month-old) male mice every 4 h over a 24-h period, and dynamic changes in cell abundance in these three myeloid compartments were quantified by fluorescence-associated cell sorting (FACS) (Fig. 1a–f and Extended Data Fig. 1). Consistent with previously published data[8], young $Ly6C^{hi}$ monocytes demonstrated robust circadian trafficking from the bone marrow to the blood and ultradian rhythms in splenic abundance of macrophages (rhythmicity assessed using JTK_CYCLE; $P=0.00026$ for bone marrow (24-h cycle), $P=0.046$ for blood (24-h cycle), $P=1$ for spleen (24-h cycle) and $P=0.00417$ for spleen (12-h cycle)). However, the circadian rhythmicity of monocyte/macrophage numbers in blood and bone marrow was completely lost in aged mice ($P=1$ for bone marrow, blood and spleen (24-h cycle) and $P=0.23$ for spleen (12-h cycle)).

Given the importance of myeloid cells in orchestrating the immune response against pathogens, we next examined diurnal variability in response to stimulation with LPS, a canonical bacterial antigen. Susceptibility to LPS-mediated mortality is diurnally regulated, with increased mortality after LPS challenge at night (ZT12, lights off)[8,12,21,22]. Consistent with this, we found that young mice injected with LPS at ZT0 (lights on) showed significantly better survival ($P=0.033$) than young mice injected at ZT12 (Fig. 1g). By contrast, aged mice did not show any difference in survival when LPS challenge occurred at ZT0 or ZT12 (Fig. 1h), suggesting the importance of circadian rhythms in the ability to recover from TLR ligand challenge and its disruption in aging.

Next, we compared the ability of young and aged primary peritoneal macrophages to engulf fluorescent *E. coli* particles every 4 h over the course of 24 h. Young macrophages showed a strong trend of rhythmic phagocytic activity over the course of 24 h ($P=0.05$ by JTK_CYCLE), with peak phagocytic activity at the beginning of

the dark phase (Fig. 1i). This diurnal variation was completely lost in aged macrophages (Fig. 1i; $P=0.643$). These results collectively indicate that the diurnal rhythmicity of myeloid cell trafficking, systemic LPS response and macrophage-mediated phagocytosis of bacteria is lost with aging.

Aging disrupts diurnal structure of the macrophage transcriptome. To understand the molecular basis underlying loss of myeloid circadian rhythmicity with age, we performed unbiased transcriptomics and compared the diurnal rhythms of peritoneal macrophages derived from young (2-month-old) and aged (20- to 22-month-old) C57BL/6J male mice collected at 4-h time intervals over 24 h (Fig. 2a and Extended Data Fig. 2a). The percentage of live macrophages was approximately 15% lower in aged mice than in young mice; however, there were no differences in macrophage enrichment at ZT0 compared to ZT12 for either age group (Extended Data Fig. 2b). RNA-sequencing (RNA-seq) expression of macrophage-specific markers was significantly higher than that of non-macrophage cell types (Extended Data Fig. 2c), indicating that samples were highly enriched for macrophages across time points and age groups. Of note, cell counts, RNA amounts, RNA integrity number (RIN) scores and the percentage of mapped genes were similar between the two age groups (Extended Data Fig. 2d–k).

We then investigated diurnal rhythms in gene expression in young and aged macrophages over the 24-h time period. JTK_CYCLE analysis[23] identified 680 genes undergoing rhythmic transcription in macrophages from young mice but only 53 genes in aged macrophages (Fig. 2b). Circadian transcription was significantly disrupted in aged macrophages (Fig. 2c), with a majority of transcripts losing rhythmicity (Fig. 2b–e). PCA of transcripts that were rhythmically expressed in young macrophages showed significant clustering by age (Fig. 2f). Moreover, within the young macrophages, we observed subclustering by time of day over the 4-h intervals, with ZT0 and ZT24 clustering together; this subclustering was not evident in aged macrophages (Fig. 2f). These findings were independent of the algorithm used to detect oscillating transcripts, because BooteJTK, MetaCycle and RAIN also detected a strong reduction in rhythmic genes in macrophages from aged mice (Extended Data Fig. 3a). Furthermore, the conclusions were unaffected by the threshold used for false discovery rate correction, as any threshold we tested yielded more oscillating genes in young macrophages than in old macrophages across all four algorithms (Extended Data Fig. 3a). A global comparison of the amplitudes of oscillating genes revealed that amplitudes of rhythmic genes were generally higher than in non-rhythmic genes, but amplitudes of rhythmic genes were equal between young and aged macrophages (Extended Data Fig. 3b).

To determine whether the loss of global transcript rhythmicity could account for abrogated rhythmic phagocytosis in aged macrophages, we focused on the CLEAR network, a class of genes central to regulation of fundamental immune functions involving lysosomal biogenesis and function, autophagy, exo- and endocytosis and phagocytosis[24,25]. We observed a striking reduction in global expression levels of CLEAR network genes in aged macrophages (Fig. 2g,h and Extended Data Fig. 4a) and significant loss of rhythmicity in genes that belong to the KEGG pathways of phagosome, lysosome and Fcγ receptor-mediated phagocytosis (Fig. 2i and Extended Data Fig. 4b). Importantly, the expression of core clock genes was not altered between ages, and the oscillations of canonical members of the molecular clock were similar between young and old macrophages (Extended Data Fig. 5). Together, these data reveal a profound loss of rhythmic transcription in macrophages during aging, including phagocytosis-related genes, while the core molecular clock is unaffected.

Chromatin structure does not account for loss of rhythmic transcription. We next tested whether the loss of oscillatory gene expression in aged macrophages was mediated by age-associated epigenetic alterations. To this end, we conducted transposase-accessible chromatin sequencing (ATAC-seq) on peritoneal macrophages collected from young and aged mice every 4 h over the course of 24 h. We integrated peak sizes of chromatin accessibility across 500-base pair (bp) regions and assigned peaks to genomic loci. A peak-calling algorithm was used to identify 67,992 peaks, or 500-bp regions of accessible chromatin, tested using DESeq2 (ref. [26]). Of the 7,098 differentially accessible peaks ($q<0.05$), 4,828 were more accessible in young macrophages, while only 2,270 were more accessible in old macrophages (Fig. 3a,b). Both PCA and hierarchical clustering of the peaks segregated the two age groups (Fig. 3c,d), indicating that age is the main factor driving the variability in chromatin openness among the samples[27,28].

To determine whether these chromatin alterations accounted for the loss of oscillatory gene expression in aged macrophages, we used three orthogonal approaches to link loci of differentially rhythmic genes to chromatin accessibility (Extended Data Fig. 6a). First, we determined whether differentially rhythmic genes were characterized by differentially accessible chromatin in young and old macrophages. To this end, we considered all 67,992 genomic regions and assigned gene loci to peaks using GREAT[29]. However, chromatin accessibility at differentially rhythmic loci was not different between young and old macrophages (Fig. 3e). We then tested whether differences in circadian gene expression might be explained by differentially accessible transcription start sites (TSSs) rather than by global ATAC-seq peaks. We therefore focused on promoter areas and TSSs of differentially rhythmic genes. While rhythmic genes in both groups showed generally higher accessibility than random genes, their accessibility was not different between young and old macrophages (Extended Data Fig. 6b). In fact, only 33 of 648 differentially rhythmic genes showed differential chromatin accessibility at the promoter (Extended Data Fig. 6c).

Given that overall chromatin accessibility was unlikely to account for differences in oscillatory gene expression between young and old macrophages, we then tested the possibility that the differential rhythmicity in gene expression between age groups might be mediated by rhythmic chromatin accessibility over the course of a day. We therefore explored the degree of rhythmicity in chromatin accessibility in both groups. However, JTK_CYCLE applied to ATAC-seq peaks in both young and aged macrophages did not reveal circadian rhythmicity (Extended Data Fig. 6d). A comparison of the unadjusted *P* value distributions for chromatin peaks (Extended Data Fig. 6e) and transcripts (Extended Data Fig. 6f) revealed that there is no enrichment of significant *P* values relative to the background uniform distribution of non-significant *P* values. These analyses led us to conclude that chromatin oscillations cannot be detected when applying the same methodological rigor as used for transcripts. These results suggest that differential 24-h oscillations in chromatin accessibility cannot explain the loss of rhythmic gene expression in aged macrophages.

KLF4 promotes rhythmic transcription in macrophages. Given that neither alterations in the core clock machinery nor differentially rhythmic chromatin accessibility provided mechanistic explanations for the circadian transcriptional reprogramming in aged macrophages, we examined whether differential binding of TFs may regulate the observed age-dependent loss of transcript oscillations. We identified candidate *trans*-acting factors using three conditions (Fig. 4a): (1) differential chromatin access between young and old macrophages, (2) differential binding to genes that show distinct oscillatory patterns between both age groups and (3) rhythmic expression of the TF that is lost in aged macrophages. Using chromVAR analysis[30] on all differentially accessible peaks, we identified TFs that showed significantly higher activity in young macrophages (Fig. 4b). Next, we assessed whether this differential TF activity

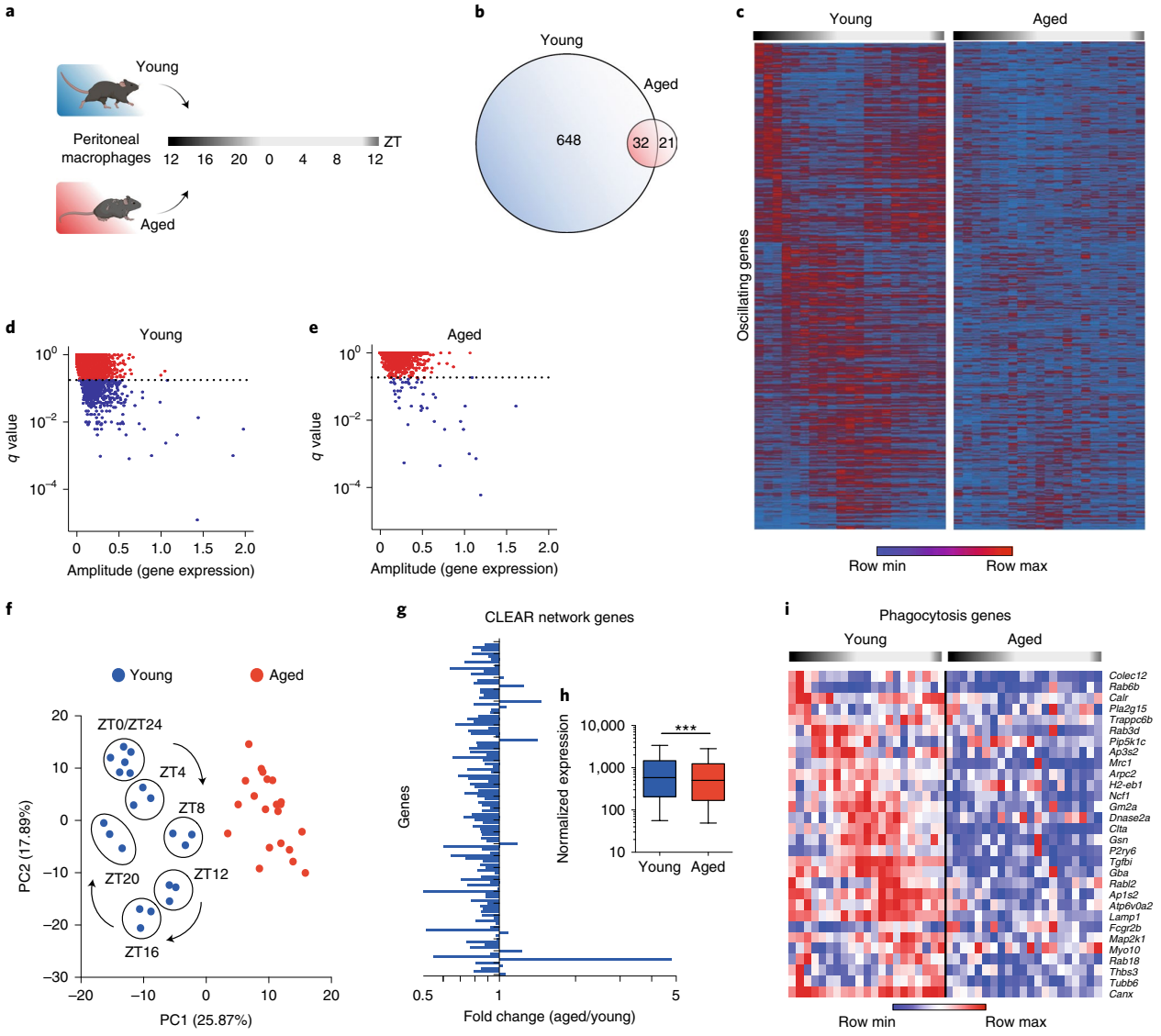

Fig. 2 | Aging abolishes rhythmic gene expression in macrophages. a, Schematic of experimental design. Peritoneal macrophages were collected from young (2-month-old) and aged (20- to 22-month-old) male mice at 4-h intervals over a 24-h period for RNA-seq; $n = 21$ mice in each age group, and $n = 3$ in each time interval. **b**, Venn diagram of unique and shared rhythmically expressed transcripts in young versus aged macrophages. **c**–**e**, Heat map of normalized expression values (**c**) and scatter plots of JTK_CYCLE results of diurnally oscillating transcripts in young (**d**) and aged (**e**) peritoneal macrophages. The dotted lines in **d** and **e** represent *q* value cutoffs of 0.2. **f**, Principal-component analysis (PCA) of rhythmic transcripts from young and aged macrophages. Note circadian clustering observed in young mice that is absent in the aged group. **g**, Fold change of normalized expression values of coordinated lysosomal expression and regulation (CLEAR) network genes in aged versus young peritoneal macrophages over all time points. **h**, Pooled normalized expression levels of CLEAR network transcripts in young and aged peritoneal macrophages; $n = 21$ mice in each age group, and $n = 3$ in each time interval; $P < 0.001$, two-sided Mann–Whitney *U*-test. Boxes extend from the 25th to 75th percentiles, whiskers extend to 1.5 times the interquartile range (IQR), and the center line is the median. **i**, A heat map of normalized expression values showing genes belonging to the KEGG pathway of phagocytosis (with $P < 0.05$, JTK_CYCLE) over a 24-h time period in young and aged peritoneal macrophages. Each column represents one mouse; $n = 3$ mice per age per time interval.

could account for the alterations in rhythmic transcription between both age groups. We focused on genes with differentially rhythmic expression and assessed TF binding activity in corresponding ATAC-seq peaks using chromVAR (Fig. 4c) and transcripts using oPossum (Fig. 4d).

The only TF that fulfilled all three criteria was the zinc finger-containing TF KLF4. KLF4 is a member of the KLF family of TFs and has been extensively investigated for its role in the regulation of cell differentiation and stem cell reprogramming[31–35]. We found that KLF4 was not only associated with differential chromatin access (Fig. 4b) and differential binding to rhythmic genes (Fig. 4c,d) but also showed oscillatory expression in young macrophages that was lost in aged cells (Fig. 4e). The properties of differential chromatin access, differential binding to rhythmic genes and rhythmic expression were unique to KLF4 among TFs and within the KLF family (Extended Data Fig. 7a,b). A de novo

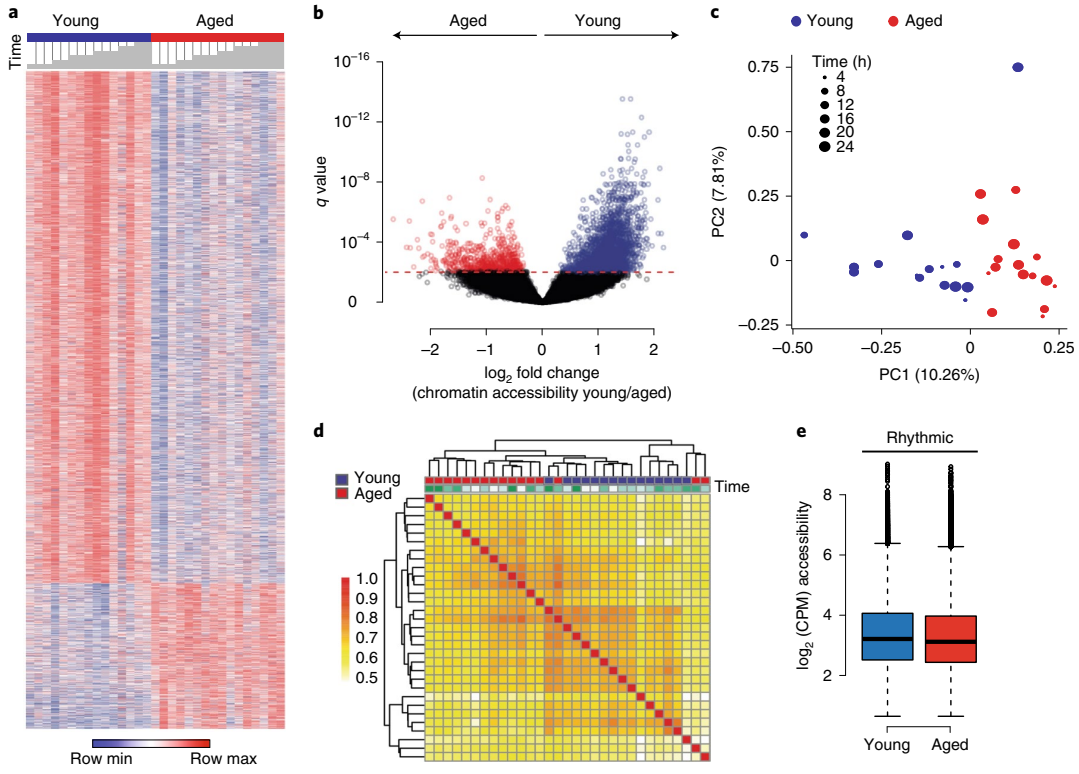

Fig. 3 | Chromatin accessibility is globally decreased in aged macrophages but does not account for loss of diurnal transcription. a, Heat map of differential chromatin accessibility peaks in young versus aged peritoneal macrophages over a 24-h cycle at 4-h intervals; $n = 15$–16 mice in each age group, and $n = 2$–3 mice per 4-h time interval. Time intervals are indicated with gray bars above the heat map starting at ZT12. Differential accessibility was determined using DESeq2. **b**, Volcano plot of differentially accessible peaks shows 4,828 versus 2,270 open chromatin peaks in young versus aged macrophages. **c**, PCA plot of accessible chromatin peaks shows separation by age between groups. **d**, Correlation matrix of Spearman correlation coefficients of chromatin accessibility between young and aged macrophages. Time is indicated by color code above the matrix, with ZT12 indicated in white and 4-h intervals represented by increasingly stronger tones of green. **e**, Chromatin accessibility (as normalized and $\log_2$-transformed values) at gene loci with rhythmic expression in young mice is not altered in aged macrophages; $n = 15$–16 mice in each age group, and $n = 2$–3 mice per 4-h time interval. Boxes extend from the 25th to 75th percentiles, whiskers extend to 1.5 times the IQR, and the center line is the median; CPM, counts per million reads mapped.

search of KLF4-binding motifs using ENCODE revealed two alternative motifs (MA0039.1 and MA0039.2), consistent with the motifs deposited in the JASPAR database (Extended Data Fig. 7c,d). Importantly, KLF4 binding to MA0039.1 was significantly higher in young macrophages across all chromatin accessible regions and peaks associated with differentially rhythmic genes (Fig. 4f,g), while binding to the MA0039.2 motif was not different between both groups (Extended Data Fig. 7e,f).

In young macrophages, diurnal increases of *Klf4* gene expression occurred at ZT12 (Fig. 4e), similar to the diurnal peak in

Fig. 4 | Age-dependent loss of KLF4 reduces macrophage circadian function. a, Schematic of selection criteria for candidate regulatory elements. **b**, Heat map of differentially accessible TF motifs in chromatin data from young versus aged macrophages over 24 h in 4-h time intervals. **c**, Heat map of differentially accessible TF motifs in chromatin data from loci with differential rhythmic expression in young versus aged macrophages over 24 h in 4-h time intervals. In **b** and **c**, for each motif, a two-sample *t*-test was performed on the chromVAR[30] deviations between young and aged samples. *P* values were adjusted for multiple hypothesis testing, and *q* values of <0.05 are highlighted along the side of the heat maps. The arrow denotes KLF4 binding to the MA0039.1 motif. **d**, Enrichment of TF motifs in rhythmic genes in young versus aged macrophages. The analysis was performed using oPossum. **e**, *Klf4* mRNA rhythmicity in young and aged macrophages; $P = 0.01$ and $P = 1$ for young and aged, respectively, JTK_CYCLE ($n = 3$ mice per age per time interval). Data represent mean ± s.e.m. **f**, chromVAR[30] deviations within all 500-bp peaks indicating KLF4 binding by estimating accessibility within peaks sharing the MA0039.1 motif or annotation; $P = 4.55 \times 10^{-6}$, two-sided Mann–Whitney *U*-test. **g**, chromVAR[30] deviations within peaks associated with differentially rhythmic genes indicating KLF4 binding by estimating accessibility within peaks sharing the MA0039.1 motif or annotation; $P = 1.25 \times 10^{-3}$, two-sided Mann–Whitney *U*-test. In **f** and **g**, boxes extend from the 25th to 75th percentiles, whiskers extend to 1.5 times the IQR, and the center line is the median; $n = 15$–16 mice in each age group and $n = 2$–3 mice per 4-h time interval. **h**, Phagocytosis of young and aged peritoneal macrophages transfected with *Klf4* short hairpin RNA (shRNA) or scrambled vector as a control; $n = 5$ mice in each group. The experiment was repeated twice. Data represent mean ± s.e.m.; $^{*}P < 0.05$ and $^{**}P < 0.005$, two-sided Mann–Whitney *U*-test. **i**, Phagocytosis of fluorescent *E. coli* particles by peritoneal macrophages from young mice treated with intraperitoneal lentiviral *Klf4* shRNA or scrambled shRNA; $P = 0.006$ and $P = 0.176$ for *Klf4* shRNA and control, respectively, by JTK_CYCLE ($n = 3$ mice per time point per group). Data represent mean ± s.e.m.

phagocytosis (Fig. 1i). Ex vivo knockdown of *Klf4* in young and aged macrophages significantly disrupted bacterial phagocytosis (Fig. 4h), indicating a central role for this TF in regulating phagocytic activity. Moreover, in vivo knockdown of *Klf4* in young peritoneal macrophages subjected to intraperitoneal lentiviral infection of *Klf4* shRNA[36] caused loss of circadian rhythmicity of *Klf4* and the phagocytosis genes *Gba* and *Rab3d* (Extended Data Fig. 8a–d) and disrupted diurnal rhythms in phagocytic activity of *E. coli* particles (Fig. 4i). Thus, knockdown of *Klf4* in young macrophages recapitulated the loss of rhythmic phagocytosis seen in aged macrophages (Fig. 1i). In addition, in vivo knockdown of *Arntl* similarly abolished circadian rhythmicity of *Klf4* and phagocytosis (Extended Data Fig. 8e–g), suggesting that *Klf4* is a clock-controlled gene that regulates circadian rhythmicity of phagocytosis.

To assess the potential clinical relevance of *Klf4* in aged macrophages, we investigated whether variants of *KLF4* might be linked to age-associated deficits in antimicrobial immunity in humans. We therefore investigated phenotypes associated with the rs2236599 genetic variant of *KLF4* (refs. [37–39]) in the UK BioBank (Supplementary Table 1). This synonymous variant leads to an adenine-to-guanine transition at Gly390 (Extended Data Fig. 8h). Carriers of this variant demonstrated a significantly elevated

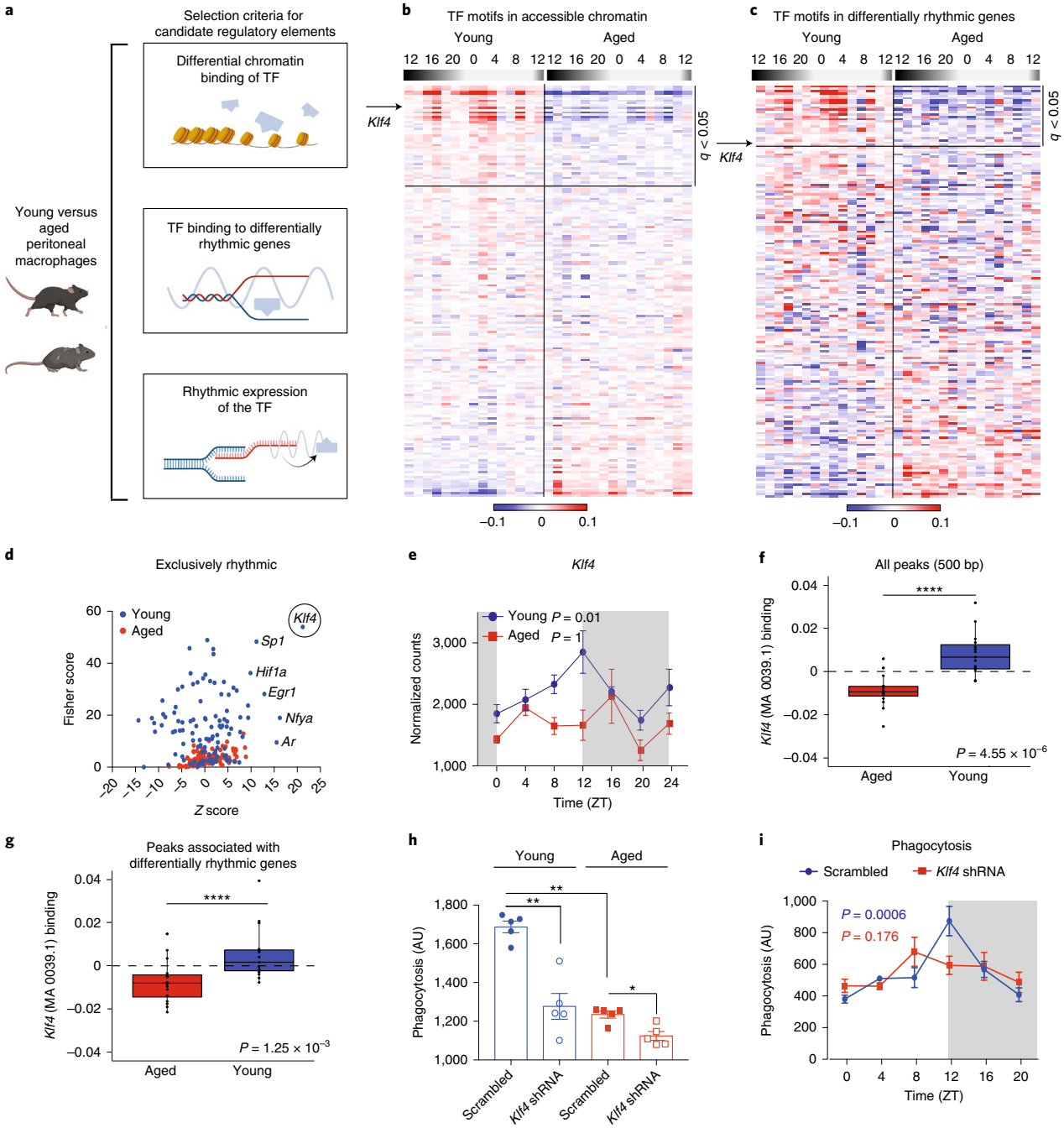

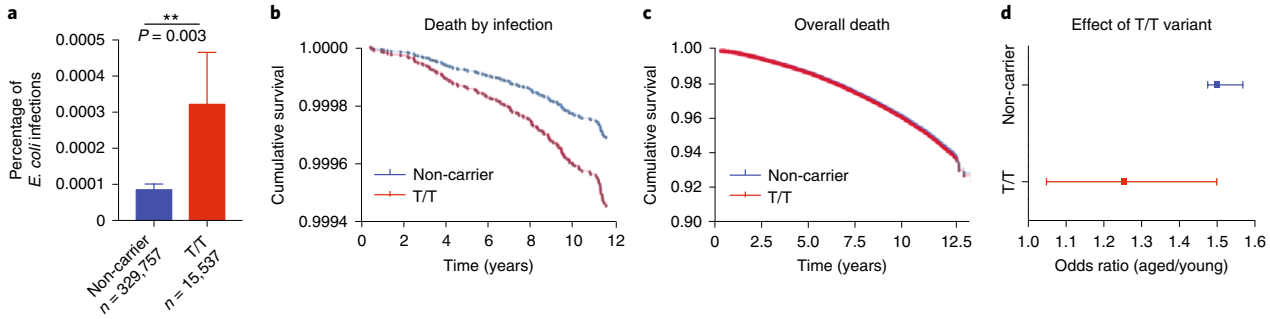

Fig. 5 | The *KLF4* variant may be linked to age-associated differences in antimicrobial immunity in humans. a, Percentages of *E. coli* infections of non-carrier versus T/T *KLF4* variant carriers using UK BioBank data analysis; $n = 329{,}757$ non-carrier and 15,537 T/T carrier individuals. Data represent mean ± s.e.m.; $P = 0.003$, univariate chi-squared test. **b**, UK BioBank data analysis of 12-year survival of non-carrier versus T/T variant carriers that succumbed to microbial infection; $n = 19{,}791$ non-carrier and 949 T/T variant carrier deceased individuals; $P = 0.089$, Cox regression adjusted for age, sex and body mass index (BMI). **c**, Overall survival of individuals is not different between non-carriers and T/T variant carriers; $n = 329{,}757$ non-carrier and 15,537 T/T variant carrier individuals; $P > 0.05$, Cox regression adjusted for age, sex and BMI. **d**, Odds ratio to develop *E. coli* infection in participants older than 65 years who carry the rs2236599 *KLF4* variant (T/T) versus in non-carriers shows that increased susceptibility to infection with age is less pronounced in individuals carrying the *KLF4* variant; $n = 266{,}771$ non-carriers younger than 65 and 62,986 older than 65; $n = 12{,}593$ T/T carrier individuals younger than 65 and 2,944 older than 65. Data show odds ratio with 95% confidence interval.

risk of developing *E. coli* infection in the entire study population (Fig. 5a). In addition, carriers of the *KLF4* variant show selectively enhanced infection-related mortality in the setting of normal overall survival (Fig. 5b,c and Supplementary Table 1). Interestingly, while non-carriers over the age of 65 years showed an elevated odds ratio to contract an *E. coli* infection compared to younger individuals, this age-associated risk was less pronounced with the *KLF4* variant (Fig. 5d). Thus, the rs2236599 genetic variant of *KLF4* reveals a significant association with susceptibility to death from bacterial infection. It furthermore indicates that carriers of the *KLF4* variant show less accentuated differences in susceptibility between young and old age. This observational analysis suggests a connection between *KLF4* and innate immune functions in humans and suggests that this process might be impacted by aging.

Discussion

Our work builds on the observation that the immune system changes significantly with aging, and the mechanisms responsible are just beginning to be explored. The aging immune system becomes skewed toward the myeloid cell lineage[19,40,41], but macrophages lose their homeostatic polarization states and phagocytic capacities, phenotypes that are driven in part by an age-associated decline in cellular energy metabolism[42]. In this study, we identify a profound loss of oscillatory gene expression in aged macrophages that is likely to further compound this functional decline. We also demonstrate that aging is characterized by loss of diurnal phagocytosis and migration of Ly6C^{hi} monocytes from bone marrow to blood; this phenotype would be expected to impair coordination of immune defenses against microbial pathogens, and in a sepsis model, diurnally controlled survival differences were abolished with aging. The core clock genes remained rhythmic in aged macrophages, and while dramatic differences were found in chromatin architecture of aged compared to young macrophages, there were no diurnal fluctuations in chromatin accessibility that could explain the loss of transcriptional rhythmicity. Rather, we identified the upstream TF KLF4, binding through a second motif distinct from that involved in cellular reprogramming, as responsible for oscillatory gene expression and phagocytic activity. Knockdown of *Klf4* expression in young macrophages recapitulated the effect of aging on rhythmic phagocytosis and phagocytic gene expression. Examination of a human genetic variant of *KLF4* revealed a significant association with age-dependent susceptibility to death from bacterial infection.

The TF KLF4 has been extensively studied in the context of somatic cell reprogramming and cell fate determination[34,35] where it binds the MA0039.2 motif[31,43]. Recent studies further indicate a role for KLF4 in the regulation of enhancer networks in cell fate transition[44]. KLF4 also functions in terminally differentiated cells in the intestinal epithelium[45], in monocyte cell differentiation[46] and in establishment of M2 macrophage polarization states[47,48]. In regulating circadian gene transcription in young macrophages, KLF4 bound to the motif MA0039.1, which is distinct from that involved in stem cell reprogramming[31,43]. We found that the MA0039.1 motif was significantly enriched in young macrophages across all open chromatin regions and peaks associated with differentially rhythmic genes, while no such enrichment was found for the MA0039.2 motif involved in cell differentiation and reprogramming. This difference may be due to different chromatin states in different cell types, pluripotency potential and age and points toward a new, context-dependent function of KLF4.

Our results indicate that while oscillations in *Klf4* transcription are *Arntl* dependent, additional, as of yet unknown, factors mediate the decline in *Klf4* oscillations with age, while rhythmicity of *Arntl* transcript levels are unaffected by age. Furthermore, it is likely that additional TFs are involved in the age-associated loss of rhythmic gene expression in macrophages.

In summary, we demonstrate a marked disruption in the circadian rhythmicity of macrophage functions and macrophage transcriptional responses with aging. It is possible that cells of the immune system, and macrophages in particular, are subject to more varied and sustained cell-extrinsic cues with aging that might disrupt coordinated immune gene expression, leading to age-associated dysregulation of diurnal and homeostatic immune functions. We also identify a new role for KLF4 as a cell-intrinsic regulator of homeostatic circadian regulation in aging macrophages.

Online content

Any methods, additional references, Nature Research reporting summaries, source data, extended data, supplementary information, acknowledgements, peer review information; details of author contributions and competing interests; and statements of data and code availability are available at https://doi.org/10.1038/s41590-021-01083-0.

Received: 2 November 2020; Accepted: 27 October 2021;
Published online: 23 December 2021

References

1. Bhadra, U., Thakkar, N., Das, P. & Pal Bhadra, M. Evolution of circadian rhythms: from bacteria to human. *Sleep Med.* **35**, 49–61 (2017).
2. Herzog, E. D. & Tosini, G. The mammalian circadian clock shop. *Semin. Cell Dev. Biol.* **12**, 295–303 (2001).
3. Storch, K. F. et al. Extensive and divergent circadian gene expression in liver and heart. *Nature* **417**, 78–83 (2002).
4. Zhang, R., Lahens, N. F., Ballance, H. I., Hughes, M. E. & Hogenesch, J. B. A circadian gene expression atlas in mammals: implications for biology and medicine. *Proc. Natl Acad. Sci. USA* **111**, 16219–16224 (2014).
5. Fonken, L. K. et al. Microglia inflammatory responses are controlled by an intrinsic circadian clock. *Brain Behav. Immun.* **45**, 171–179 (2015).
6. He, W. et al. Circadian expression of migratory factors establishes lineage-specific signatures that guide the homing of leukocyte subsets to tissues. *Immunity* **49**, 1175–1190 (2018).
7. Keller, M. et al. A circadian clock in macrophages controls inflammatory immune responses. *Proc. Natl Acad. Sci. USA* **106**, 21407–21412 (2009).
8. Nguyen, K. D. et al. Circadian gene *Bmal1* regulates diurnal oscillations of Ly6C^{hi} inflammatory monocytes. *Science* **341**, 1483–1488 (2013).
9. Geiger, S. S., Curtis, A. M., O'Neill, L. A. J. & Siegel, R. M. Daily variation in macrophage phagocytosis is clock-independent and dispensable for cytokine production. *Immunology* **157**, 122–136 (2019).
10. Kitchen, G. B. et al. The clock gene *Bmal1* inhibits macrophage motility, phagocytosis, and impairs defense against pneumonia. *Proc. Natl Acad. Sci. USA* **117**, 1543–1551 (2020).
11. Oliva-Ramírez, J., Moreno-Altamirano, M. M. B., Pineda-Olvera, B., Cauich-Sánchez, P. & Javier Sánchez-García, F. Crosstalk between circadian rhythmicity, mitochondrial dynamics and macrophage bactericidal activity. *Immunology* **143**, 490–497 (2014).
12. Curtis, A. M. et al. Circadian control of innate immunity in macrophages by miR-155 targeting *Bmal1*. *Proc. Natl Acad. Sci. USA* **11**, 7231–7236 (2015).
13. Hayashi, M., Shimba, S. & Tezuka, M. Characterization of the molecular clock in mouse peritoneal macrophages. *Biol. Pharm. Bull.* **30**, 621–626 (2007).
14. Knyszynski, A. & Fischer, H. Circadian fluctuations in the activity of phagocytic cells in blood, spleen, and peritoneal cavity of mice as measured by zymosan-induced chemiluminescence. *J. Immunol.* **127**, 2508–2511 (1981).
15. Leone, M. J., Marpegan, L., Duhart, J. M. & Golombek, D. A. Role of proinflammatory cytokines on lipopolysaccharide-induced phase shifts in locomotor activity circadian rhythm. *Chronobiol. Int.* **29**, 715–723 (2012).
16. Rahman, S. A. et al. Endogenous circadian regulation of pro-inflammatory cytokines and chemokines in the presence of bacterial lipopolysaccharide in humans. *Brain Behav. Immun.* **47**, 4–13 (2015).
17. Huo, M. et al. Myeloid *Bmal1* deletion increases monocyte recruitment and worsens atherosclerosis. *FASEB J.* **31**, 1097–1106 (2017).
18. Scheiermann, C., Kunisaki, Y. & Frenette, P. S. Circadian control of the immune system. *Nat. Rev. Immunol.* **13**, 190–198 (2013).
19. Rossi, D. J., Jamieson, C. H. & Weissman, I. L. Stems cells and the pathways to aging and cancer. *Cell* **132**, 681–696 (2008).
20. Liu, Q. et al. Peripheral TREM1 responses to brain and intestinal immunogens amplify stroke severity. *Nat. Immunol.* **20**, 1023–1034 (2019).
21. Deng, W. et al. The circadian clock controls immune checkpoint pathway in sepsis. *Cell Rep.* **24**, 366–378 (2018).
22. Scheiermann, C. et al. Adrenergic nerves govern circadian leukocyte recruitment to tissues. *Immunity* **37**, 290–301 (2012).
23. Hughes, M. E., Hogenesch, J. B. & Kornacker, K. JTK-CYCLE: an efficient nonparametric algorithm for detecting rhythmic components in genome-scale data sets. *J. Biol. Rhythms* **25**, 372–380 (2010).
24. Palmieri, M. et al. Characterization of the CLEAR network reveals an integrated control of cellular clearance pathways. *Hum. Mol. Genet.* **20**, 3852–3866 (2011).
25. Sardiello, M. et al. A gene network regulating lysosomal biogenesis and function. *Science* **325**, 473–477 (2009).
26. Love, M. I., Huber, W. & Anders, S. Moderated estimation of fold change and dispersion for RNA-seq data with DESeq2. *Genome Biol.* **15**, 550–550 (2014).
27. Moskowitz, D. M. et al. Epigenomics of human CD8 T cell differentiation and aging. *Sci. Immunol.* **2**, eaag0192 (2017).
28. Ucar, D. et al. The chromatin accessibility signature of human immune aging stems from CD8$^+$ T cells. *J. Exp. Med.* **214**, 3123–3144 (2017).
29. McLean, C. Y. et al. GREAT improves functional interpretation of *cis*-regulatory regions. *Nat. Biotechnol.* **28**, 495–501 (2010).
30. Schep, A. N., Wu, B., Buenrostro, J. D. & Greenleaf, W. J. ChromVAR: inferring transcription-factor-associated accessibility from single-cell epigenomic data. *Nat. Methods* **14**, 975–978 (2017).
31. Chen, X. et al. Integration of external signaling pathways with the core transcriptional network in embryonic stem cells. *Cell* **133**, 1106–1117 (2008).
32. Maherali, N. et al. Directly reprogrammed fibroblasts show global epigenetic remodeling and widespread tissue contribution. *Cell Stem Cell* **1**, 55–70 (2007).
33. Okita, K., Ichisaka, T. & Yamanaka, S. Generation of germline-competent induced pluripotent stem cells. *Nature* **448**, 313–317 (2007).
34. Takahashi, K. & Yamanaka, S. Induction of pluripotent stem cells from mouse embryonic and adult fibroblast cultures by defined factors. *Cell* **126**, 663–676 (2006).
35. Wernig, M. et al. In vitro reprogramming of fibroblasts into a pluripotent ES-cell-like state. *Nature* **448**, 318–324 (2007).
36. Ipseiz, N. et al. Effective in vivo gene modification in mouse tissue-resident peritoneal macrophages by intraperitoneal delivery of lentiviral vectors. *Mol. Ther. Methods Clin. Dev.* **16**, 21–31 (2020).
37. Liu, H. et al. Irf6 directly regulates Klf17 in zebrafish periderm and Klf4 in murine oral epithelium, and dominant-negative *KLF4* variants are present in patients with cleft lip and palate. *Hum. Mol. Genet.* **25**, 766–776 (2016).
38. Stratopoulos, A. et al. Genomic variants in members of the Krüppel-like factor gene family are associated with disease severity and hydroxyurea treatment efficacy in β-hemoglobinopathies patients. *Pharmacogenomics* **20**, 791–801 (2019).
39. Stremitzer, S. et al. Genetic variants associated with colorectal brain metastases susceptibility and survival. *Pharmacogenomics J.* **17**, 29–35 (2017).
40. Soufi, A. et al. Pioneer transcription factors target partial DNA motifs on nucleosomes to initiate reprogramming. *Cell* **161**, 555–568 (2015).
41. Di Giammartino, D. C. et al. KLF4 is involved in the organization and regulation of pluripotency-associated three-dimensional enhancer networks. *Nat. Cell Biol.* **21**, 1179–117 (2019).
42. McConnell, B. B., Ghaleb, A. M., Nandan, M. O. & Yang, V. W. The diverse functions of Krüppel-like factors 4 and 5 in epithelial biology and pathobiology. *BioEssays* **29**, 549–557 (2007).
43. Alder, J. K. et al. Kruppel-like factor 4 is essential for inflammatory monocyte differentiation in vivo. *J. Immunol.* **180**, 5645–5652 (2008).
44. Kapoor, N. et al. Transcription factors STAT6 and KLF4 implement macrophage polarization via the dual catalytic powers of MCPIP. *J. Immunol.* **194**, 6011–6023 (2015).
45. Liao, X. et al. Krüppel-like factor 4 regulates macrophage polarization. *J. Clin. Invest.* **121**, 2736–2749 (2011).
46. Dykstra, B. & de Haan, G. Hematopoietic stem cell aging and self-renewal. *Cell Tissue Res.* **331**, 91–101 (2008).
47. Dykstra, B., Olthof, S., Schreuder, J., Ritsema, M. & de Haan, G. Clonal analysis reveals multiple functional defects of aged murine hematopoietic stem cells. *J. Exp. Med.* **208**, 2691–2703 (2011).
48. Minhas, P. S. et al. Macrophage de novo NAD$^+$ synthesis specifies immune function in aging and inflammation. *Nat. Immunol.* **20**, 50–63 (2019).

Methods

Animals. This study was conducted in accordance with National Institutes of Health (NIH) guidelines; protocols were approved by the Institutional Animal Care and Use Committee at Stanford University. Young (2- to 3-month-old; Jackson Laboratories) and aged (20- to 22-month-old; National Institute of Aging) C57BL/6J male mice were housed in an environment-controlled, pathogen-free barrier facility on a 12-h/12-h light/dark cycle at a constant temperature and humidity, with food and water available ad libitum.

Flow cytometry. Young and aged mice were terminally anesthetized (100 mg kg^{-1} ketamine and 10 mg kg^{-1} xylazine intraperitoneally) at 4-h intervals over the course of 24 h. Blood samples were collected retro-orbitally, diluted 1:4 in PBS without Ca^{2+}/Mg^{2+}, centrifuged over a Ficoll gradient to remove granulocytes and red blood cells (RBCs) and washed once with PBS. Bone marrow cells were flushed from tibias, and spleens were homogenized and filtered through a 40-µm strainer to remove large cellular debris. Single-cell suspensions of bone marrow, blood and spleen samples were subjected to RBC lysis and washed with PBS. Cells were then stained with antibodies (1:200 dilution) for 45 min on ice against CD45 (clone 30-F11, 103127), CD11b (clone M1/70, 101245), Ly6C (clone HK1.4, 128016), Ly6G (clone 1A8, 127623), CD115 (clone AF598, 135517), CD3 (clone 17A2, 100204), CD19 (clone 6D5, 115520) and F4/80 (clone BM8, 123128) from BioLegend and analyzed on a BD-LSR II cytometer with FlowJo software, version 10.6.1.

LPS administration. Mice were maintained in a controlled light/dark environment for 2 weeks before LPS challenge. Mice were injected intraperitoneally either at ZT0 or ZT12 with LPS derived from *E. coli* serotype 055:B5 (Sigma-Aldrich) in sterile PBS at 25 mg kg^{-1} and monitored for 1 week. The probability of survival was calculated using the Kaplan–Meier method, and statistical analysis was performed using a log-rank test.

Macrophage isolation. Peritoneal macrophages were collected from anesthetized young and aged mice every 4 h over the course of 24 h by flushing the peritoneal cavity with 10 ml of ice-cold PBS[49,50]. Miltenyi Cd11b magnetic microbeads were incubated with peritoneal macrophages for 10 min at 4 °C and then passed through a Miltenyi MS column according to the manufacturer's protocol to enrich for macrophages.

RNA-seq. *Library preparation.* Samples were lysed in Invitrogen TRIzol reagent, and RNA was isolated using Invitrogen PureLink RNA Micro columns. RNA samples were converted into Illumina libraries by using the Lexogen Quantseq Forward kit. Approximately 250 ng of total RNA was reverse transcribed using oligo(dT) priming to bias fragments toward the 3′ end of RNA fragments. cDNA fragments were converted to double-stranded cDNA and subjected to ligation of sequencing adapters and PCR amplification. All samples were pooled into a single group and sequenced on four lanes of an Illumina HiSeq 2000 with the 50-bp single-end chemistry. RNA quality and quantity and sequencing quality did not differ significantly between age groups or time points.

RNA-seq analysis. Fastq files of the raw RNA-seq reads were trimmed with Bbduk and then aligned to the mouse reference genome (mm10) with STAR using parameters as described in the Lexogen Quantseq protocol[51]. Reads were counted using HTSeq. For PCA analysis, counts were library size normalized. For evaluation of circadian rhythmicity using JTK_CYCLE, reads were library size normalized and $\log_2$ transformed using the CPM command in R. Where individual genes are plotted with normalized expression values, corresponding JTK_CYCLE *P* values were calculated using the same normalized data. Only genes with mean $\log_2$(CPM) expression of >3 were evaluated by JTK_CYCLE. KEGG pathway enrichment was performed using the 'kegga' command in limma. oPossum was used to identify TFs enriched in the promoter regions of differentially rhythmic genes.

In vivo lentiviral transduction of shRNA *Klf4* and shRNA *Arntl*. In vivo knockdown of *Klf4* and *Arntl* in peritoneal macrophages was performed as previously described[36]. High-titer lentivirus solutions were obtained from Systems Biosciences for *Arntl* shRNA (5′-GACACCTCGCAGAATGTCACAGG CAAGTT-3′), *Klf4* shRNA (5′-CATGTTCTAACAGCCTAAATG-3′) and scrambled shRNA (pGreenPuro Scramble Hairpin Control) at a concentration of $>10^8$ infectious units per ml. Lentivirus infectivity was validated in vitro using Jurkat T cells (clone E6-1, ATCC, TIB-152), as previously described[36]. One hundred microliters of *Klf4* shRNA, *Arntl* shRNA or scrambled shRNA lentivirus solutions were injected intraperitoneally into young (8-week-old) mice ($n=18$ mice per experimental group or $n=3$ mice per 4-h time point). The mice were returned to their 12-h light/12-h dark cycle with food and water available ad libitum and allowed to recover for 3 d, and peritoneal macrophages were then isolated every 4 h across 24 h.

Quantitative real-time PCR. RNA was isolated using Invitrogen TRIzol and purified with Invitrogen Purelink RNA Micro columns or with a chloroform–phenol protocol. cDNA was generated from 300 ng of RNA by using the Applied Biosystems High Capacity RT kit. Quantitative real-time PCR (qRT–PCR) was performed on a QuantStudio6 using TaqMan primers for *Arntl* (Mm00500226_m1), *Per2* (Mm00478099_m1) and *Gapdh* (Mm99999915_g1). Relative expression was measured using the $\Delta\Delta C_t$ method with *Gapdh* or *18S* (forward: 5′-CTTAGAGGG ACAAGTGGCG-3′; reverse: 5′-ACGCTGAGCCAGTCAGTGTA-3′) as endogenous references. To assess gene expression in peritoneal macrophages isolated from mice treated with lentivirus containing either *Klf4* shRNA, *Arntl* shRNA or scrambled shRNA, the following primers were used from Origene: *Klf4* (MP207225: forward, 5′-CTATGCAGGCTGTGGCAAAACC-3′; reverse, 5′-TTG CGGTAG TGCCTGGTCAGTT-3′), *Arntl* (MP200931: forward, 5′-ACCTCGCA GAATGTCACAGGCA-3′; reverse, 5′-CTGAACCATCGACTTCGTAGCG-3′), *Gba* (MP222451: forward, 5′-GCCAGTTGTGACTTCTCCATCC-3′; reverse, 5′-CGTGAGGACATCTTCAGGGCTT-3′) and *Rab3d* (MP212343: forward, 5′-ATGACATCGCCAACCAGGAGTC-3′; reverse, 5′-CGTTCGTCTTCCAGG TCACACT-3′).

Phagocytosis assay. Macrophage phagocytic activity of peritoneal macrophages was assessed using the Vybrant Phagocytosis Assay kit (Thermo Fisher Scientific), according to the manufacturer's instructions. Briefly, macrophages were isolated from the peritoneum as described above and cultured in 96-well black culture plates at 10^6 cells per well for 2 h. Culture medium was removed, and fluorescein-labeled *E. coli* BioParticles or PBS was added. After 2 h, supernatant was removed, and 100 µl of trypan blue was immediately added to each well for 1 min to quench extracellular fluorescence. Excess trypan blue dye was removed by aspiration. The plate was read on a SpectraMax M2e microplate reader (Molecular Devices; excitation of 480 nm and emission of 520 nm; bottom reading with 50 flashes per well).

ATAC-seq transposase reaction, library generation and sequencing. Peritoneal macrophages were isolated every 4 h over the course of 24 h from young and aged mice, washed with cold PBS at 4 °C and centrifuged at 500*g* for 5 min. The cell pellet was resuspended in Tn5 transposase reaction mix (25 µl of 2× TD buffer, 2.5 µl of Tn5 transposase and 22.5 µl of nuclease-free water) and incubated at 37 °C for 30 min with mild agitation. DNA from the transposase reaction was purified using the DNA Clean & Concentrator kit (Zymo, D4014) and PCR amplified as described in ref. [52]. Fragment analysis was run on the PCR products using NGS Fragment 1–6,000 bp (Agilent) as a quality control step and to construct the library. The library was then sequenced on a Illumina HiSeq 4000 instrument as 2×100 mers.

Analysis of ATAC-seq data. *Data processing.* Fastq files were trimmed using Trim Galore! (version 0.6.4_dev; parameters: –stringency 5) and aligned to the mm10 genome using Bowtie2 (version 2.3.4.1; parameters: –very-sensitive-local–dovetail–no-discordant–no-mixed). The following reads were filtered out: reads aligning to the mitochondrial genome (samtools idxstats {in_path} | cut -f 1 | grep -v chrM | xargs samtools view -b {in_path} > out_path}), PCR duplicates (java -jar $PICARD_JAR MarkDuplicates I={in_path} O={out_path} M={out_metrics_ path} REMOVE_DUPLICATES=true) and reads aligning to ENCODE blacklisted regions (samtools view -f 2 -q 20 -b {in_path} | bedtools intersect -v -abam–b mm10-blacklist.v2.bed -wa > {out_path}).

Creating ATAC-seq count matrices. For each sample, ChrAccR (https://greenleaflab.github.io/ChrAccR/articles/overview.html) was used to count the number of fragments (transposase cut site centered) within preselected genomic regions. We created two different count matrices: one in which fragments were counted within open chromatin regions as determined by a peak-calling algorithm and one in which fragments were counted within the 4,000 bp surrounding each TSS. Peaks were called using Genrich (version 0.6; all default parameters), which considers all replicates of the same condition together. Only peaks with a *q* value of <0.05 were retained, and these variable-width peaks were merged across all samples (bedtools version 2.2.9.2). For each merged peak, the summit of the constituent peak with the most significant *q* value was identified. Around each of these summits, a 500-bp region was extracted, resulting in $n=67{,}992$ regions with a fixed width of 500 bp. For all but the DESeq2 analyses, these matrices were library size normalized (CPM) and then $\log_2$ transformed using the CPM command in R[53].

Downstream analysis. PCA was performed on the library size-normalized and $\log_2$-transformed matrices. DESeq2 (version 1.28.1) was run using the following design formula: ~time + age + time:age, with age as the main effect and time point as a covariate. Genomic regions were associated with genes using GREAT[29].

Estimating TF-binding motif enrichment. chromVAR[30] was used to quantify TF activity in $n=176$ motifs from the JASPAR2018 database.

UK BioBank study population. The UK BioBank study is a large, multisite, community-based cohort study with the overarching aim of improving the prevention, detection and treatment of a wide range of serious and life-threatening diseases. The study invited individuals aged 40 to 69 years to take part. All UK residents aged 40 to 69 years who were registered with the National Health Service

and living up to 25 miles from 1 of the 22 study assessment centers were invited to participate. All participants gave informed consent for genotyping and data linkage to medical reports. Genotyping of the *KLF4* variant rs2236599 was conducted in a total of 488,377 individuals. Ongoing inpatient hospital records beginning in 1996 were used to identify diagnoses according to the International Classification of Diseases, Tenth Revision (ICD-10) codes. The presence of the following ICD-10 codes was evaluated: infection with *E. coli* (A04) and overall infections (A00-A99). The UK BioBank receives death notifications (age at death and primary ICD diagnosis that led to death) through linkage to national death registries. End of follow-up was defined as death or end of hospital inpatient data collection in June 2020. Specific causes of death included death by infection (A00-A99) and death by *E. coli* infection (A04). Detailed information about the study is available at the UK BioBank website (www.ukbiobank.ac.uk). The study has been approved by the UKB Access Committee (project 59657).

Statistical analysis. Three to five biological replicates were used for each experiment. Data are presented as the mean ± s.e.m. using GraphPad Prism version 7, unless otherwise stated. No statistical methods were used to predetermine sample sizes, but our sample sizes are similar to those reported in previous publications[8]. No outliers were excluded in our analyses. All patterns of rhythmicity (for example, in gene expression, FACS analysis, phagocytic activity and chromatin accessibility) were assessed using JTK_CYCLE[23], which was parameterized to look for rhythms of exactly 24 h. We compared JTK_CYCLE to three other methods of detecting rhythmicity: RAIN[54], BooteJTK[55] and MetaCycle[56]. All algorithms were instructed to find periods of exactly 24 h and run with default parameters. Multiple hypothesis correction was performed with the Benjamini–Hochberg procedure. Features with adjusted *P* values less than 0.2 were considered significantly rhythmic.

Reporting Summary. Further information on research design is available in the Nature Research Reporting Summary linked to this article.

Data availability

Transcriptomics data are available under accession number GSE128830 and at Token (ybqjocoontgtluf); ATAC-seq data are available at https://purl.stanford.edu/rc797bt9574. The dataset used for the analyses in the UK BioBank have not been deposited in a public repository but are available after approval of a reasonable application at https://www.ukbiobank.ac.ukl. Source data are provided with this paper.

References

49. Misharin, A. V., Saber, R. & Perlman, H. Eosinophil contamination of thioglycollate-elicited peritoneal macrophage cultures skews the functional readouts of in vitro assays. *J. Leukoc. Biol.* **92**, 325–331 (2012).
50. Zhang, X., Goncalves, R. & Mosser, D. M. The isolation and characterization of murine macrophages. *Curr. Protoc. Immunol.* **14**, Unit 14.1 (2008).
51. Dobin, A. et al. STAR: ultrafast universal RNA-seq aligner. *Bioinformatics* **29**, 15–21 (2013).
52. Anders, S. & Huber, W. Differential expression analysis for sequence count data. *Genome Biol.* **11**, R106–R106 (2010).
53. Robinson, M. D., McCarthy, D. J. & Smyth, G. K. edgeR: a Bioconductor package for differential expression analysis of digital gene expression data. *Bioinformatics* **26**, 139–140 (2010).
54. Thaben, P. F. & Westermark, P. O. Detecting rhythms in time series with RAIN. *J. Biol. Rhythms* **29**, 391–400 (2014).
55. Hutchison, A. L., Allada, R. & Dinner, A. R. Bootstrapping and empirical Bayes methods improve rhythm detection in sparsely sampled data. *J. Biol. Rhythms* **33**, 339–349 (2018).
56. Wu, G., Anafi, R. C., Hughes, M. E., Kornacker, K. & Hogenesch, J. B. MetaCycle: an integrated R package to evaluate periodicity in large scale data. *Bioinformatics* **32**, 3351–3353 (2016).
57. Waterhouse, A. et al. SWISS-MODEL: homology modelling of protein structures and complexes. *Nucleic Acids Res.* **46**, W296–W303 (2018).

Acknowledgements

This work was supported by RO1AG048232 (K.I.A.), RF1AG058047 (K.I.A.), the American Heart Association 19PABH134580007 (K.I.A.), RO1NS100180 (K.I.A.), 1P30 AG066515 (K.I.A.), The Zhang-Jiang Research Fund, T32 Neuroscience Institute (C.T.), NSF GRFP (C.T.), DP2AG067492 (C.A.T.), the Edward Mallinckrodt, Jr. Foundation (C.A.T.), UPenn Institute for Immunology (C.A.T.), UPenn Diabetes Research Center P30-DK-019525 (C.A.T.), Pew Biomedical Scholarship (C.A.T.), Fritz Thyssen Foundation (C.A.T.) and the UPenn Institute on Aging (C.A.T.), Marie Skłodowska-Curie Grant 888494 (E.B.), Stanford School of Medicine Dean's Postdoctoral Fellowship (E.B.), Medical Scientist Training Program T32 GM07170 (L.L.) and Training Grant in Computational Biology 5-T32-HG-000046-21 (L.L.). We thank L. de Lecea for support in housing mice, the Stanford Shared FACS facility for flow cytometry analysis on LSR instruments (S10RR027431-01) and SCGPM for sequencing on a HiSeq 2000. The ATAC-seq sequencing data were generated on an Illumina HiSeq 4000 that was purchased with funds from NIH S10OD018220 for the Stanford Functional Genomics Facility. Schematic illustrations were created with BioRender.com.

Author contributions

E.B. designed, performed and interpreted the experiments and wrote the manuscript. C.T. conceived the study, performed and analyzed RNA-seq experiments and wrote the manuscript. L.L., Z.S., K.M.S. and V.M. performed computational analyses. C.A.I. assisted with FACS and qRT–PCR experiments. B.C. and H.C.H. assisted with circadian experiments. K.I.A. and C.A.T. conceived the study, supervised the participants, interpreted the experiments and wrote the manuscript.

Competing interests

The authors declare no competing interests.

Additional information

Extended data is available for this paper at https://doi.org/10.1038/s41590-021-01083-0.

Supplementary information The online version contains supplementary material available at https://doi.org/10.1038/s41590-021-01083-0.

Correspondence and requests for materials should be addressed to Christoph A. Thaiss or Katrin I. Andreasson.

Peer review information *Nature Immunology* thanks Nicolas Cermakian, Anne Curtis, Lora Hooper, Luz Navarro and the other, anonymous, reviewer(s) for their contribution to the peer review of this work. L.A. Dempsey was the primary editor on this article and managed its editorial process and peer review in collaboration with the rest of the editorial team.

Reprints and permissions information is available at www.nature.com/reprints.

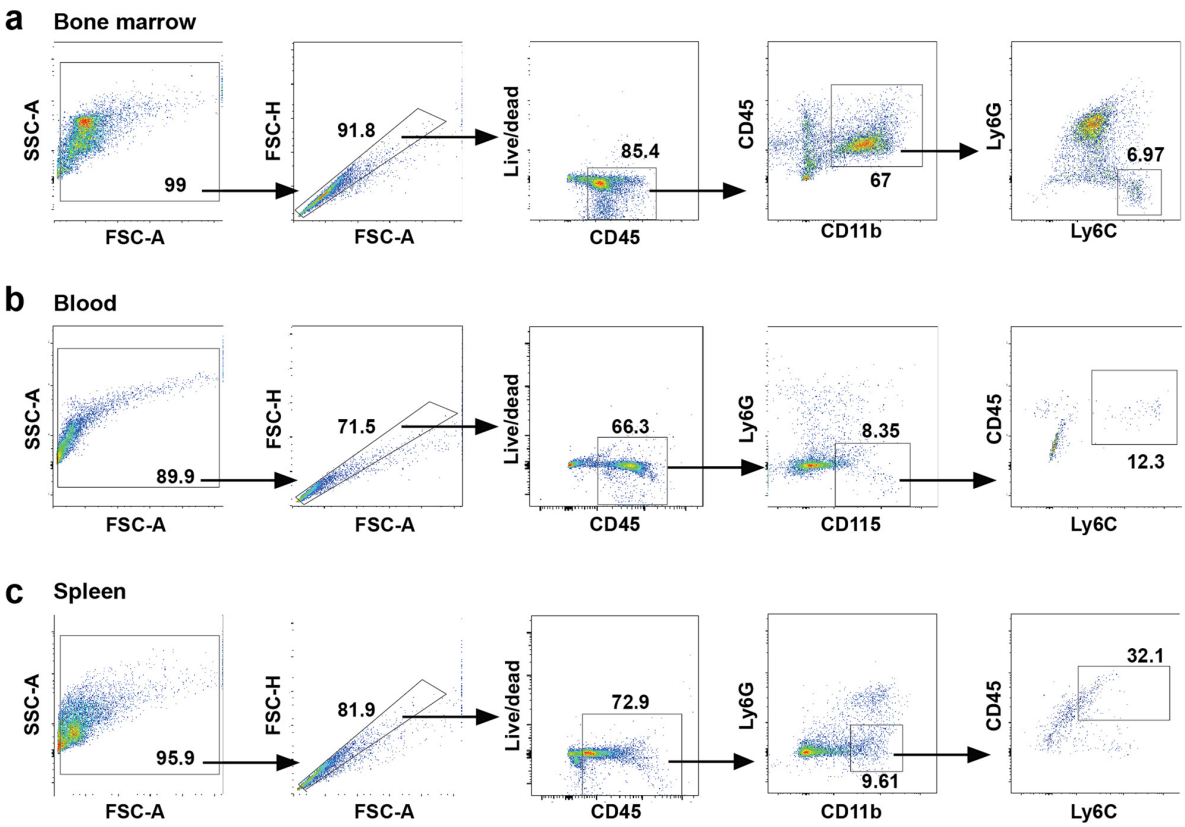

Extended Data Fig. 1 | Gating strategy for monocytes and macrophages in bone marrow, blood and spleen. Mononuclear cells from bone marrow (**a**) blood (**b**) and spleen (**c**) were gated for forward and side-scatter (FSC/SSC), doublets, and live/dead prior to identification of bone marrow (CD45 + CD11b + Ly6G-Ly6C +), blood (CD45 + CD115 + Ly6G-) and splenic (CD45 + CD11b + Ly6G-) monocytes and macrophages.

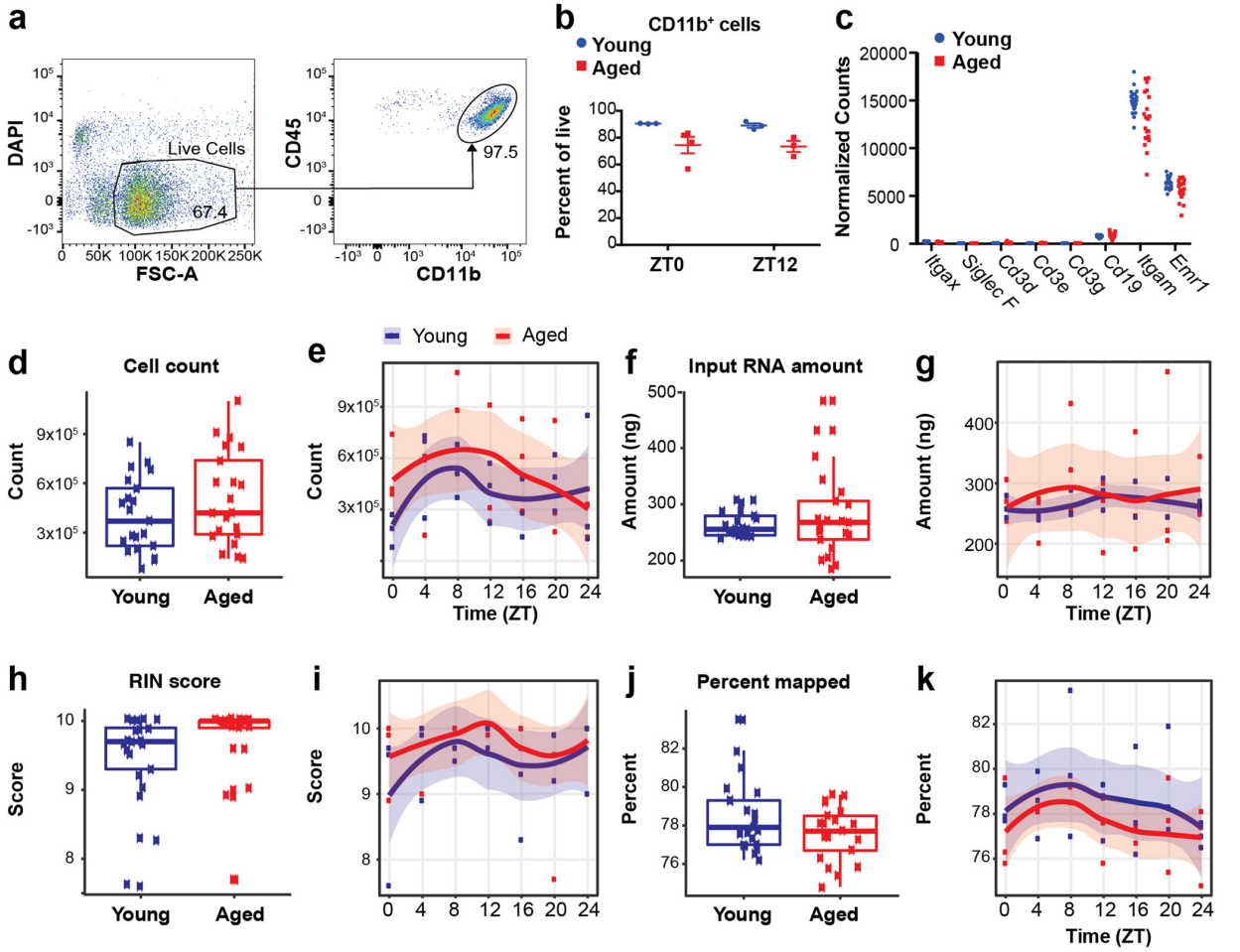

Extended Data Fig. 2 | Macrophage enrichment validation and RNA-seq quality control and analysis. a. Gating strategy for measurement of macrophage enrichment of samples at ZT0 and ZT12. **b**. Percent of live Cd11b+ macrophages in young vs aged at ZT0 and ZT12 (n = 3, 2-way ANOVA age factor p = 0.0065). **c**. Expression levels of macrophage transcripts, Itgam and Emr1 versus markers of dendritic cells (Itgax), eosinophils (Siglec F), T cells (Cd3d, Cd3e, Cd3g), and B cells (Cd19). Data are mean ± s.e.m, two-sided Mann-Whitney U test. n = 21 mice in each age group and n = 3 in each time group. **d-k**. Pooled values (d, f, h, j) and time-dependent presentations (e, g, i, k) of sample total cell counts (d-e), input RNA quantity (f-g), RIN scores (h-i) and number of mapped reads (j-k) of circadian RNA-seq analysis of young and aged peritoneal macrophages. (d, f, h, j) Data are mean ± s.e.m, two-sided Mann-Whitney U test. n = 21 mice in each age group and n = 3 in each time group. (e, g, i, k) Lines of best fit were determined using loess, and 95% confidence intervals are shown.

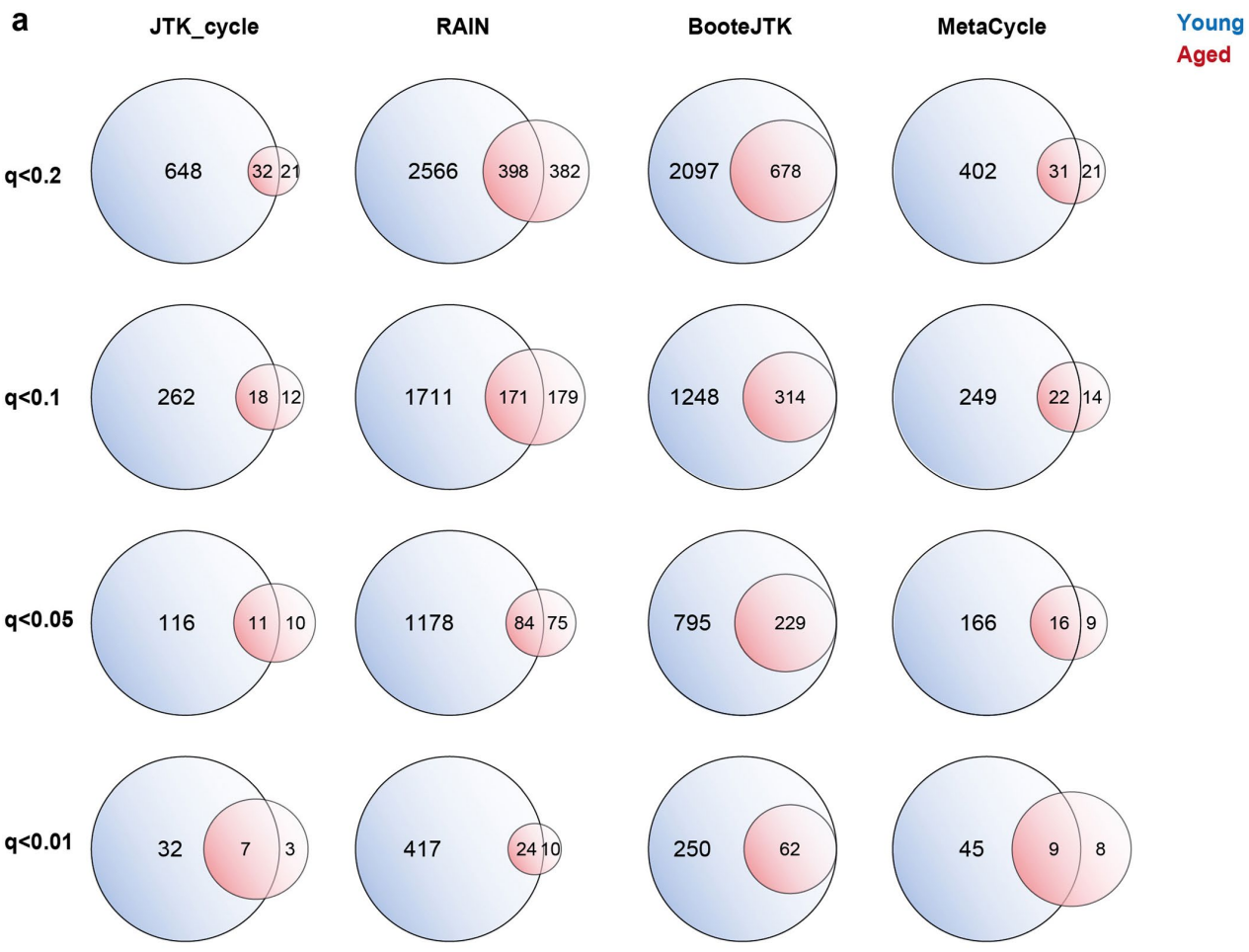

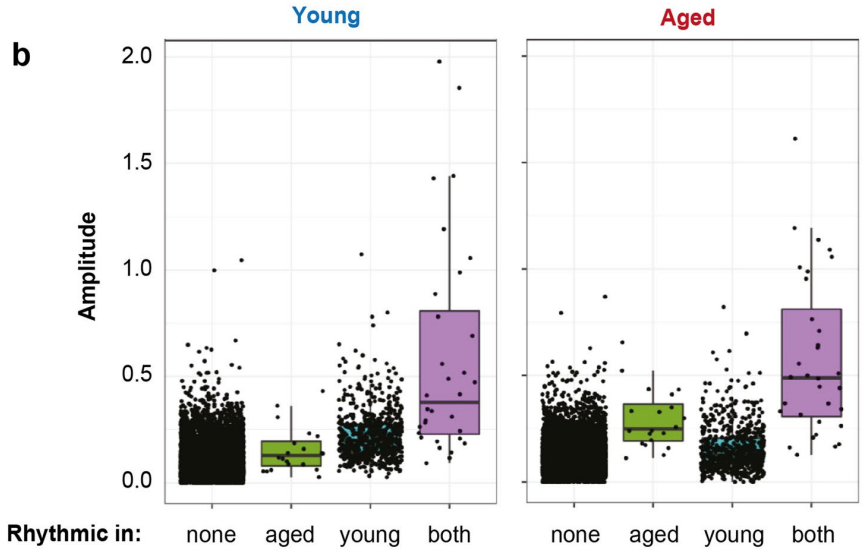

Extended Data Fig. 3 | Algorithm comparison and amplitude assessment for rhythmic transcripts. a. Venn diagrams of unique and shared rhythmically expressed transcripts in young vs. aged macrophages, compared across different algorithms (JTK_CYCLE, RAIN, BooteJTK, and MetaCycle) and q-values. **b**. JTK_CYCLE amplitudes of genes in peritoneal macrophages from young and aged mice. Genes are binned by their rhythmicity in neither, both, or individual groups. n = 21 mice in each age group and n = 3 in each time group. Boxes extend from the 25th-75th percentiles, whiskers extend to 1.5 times the IQR, and the center line is the median.

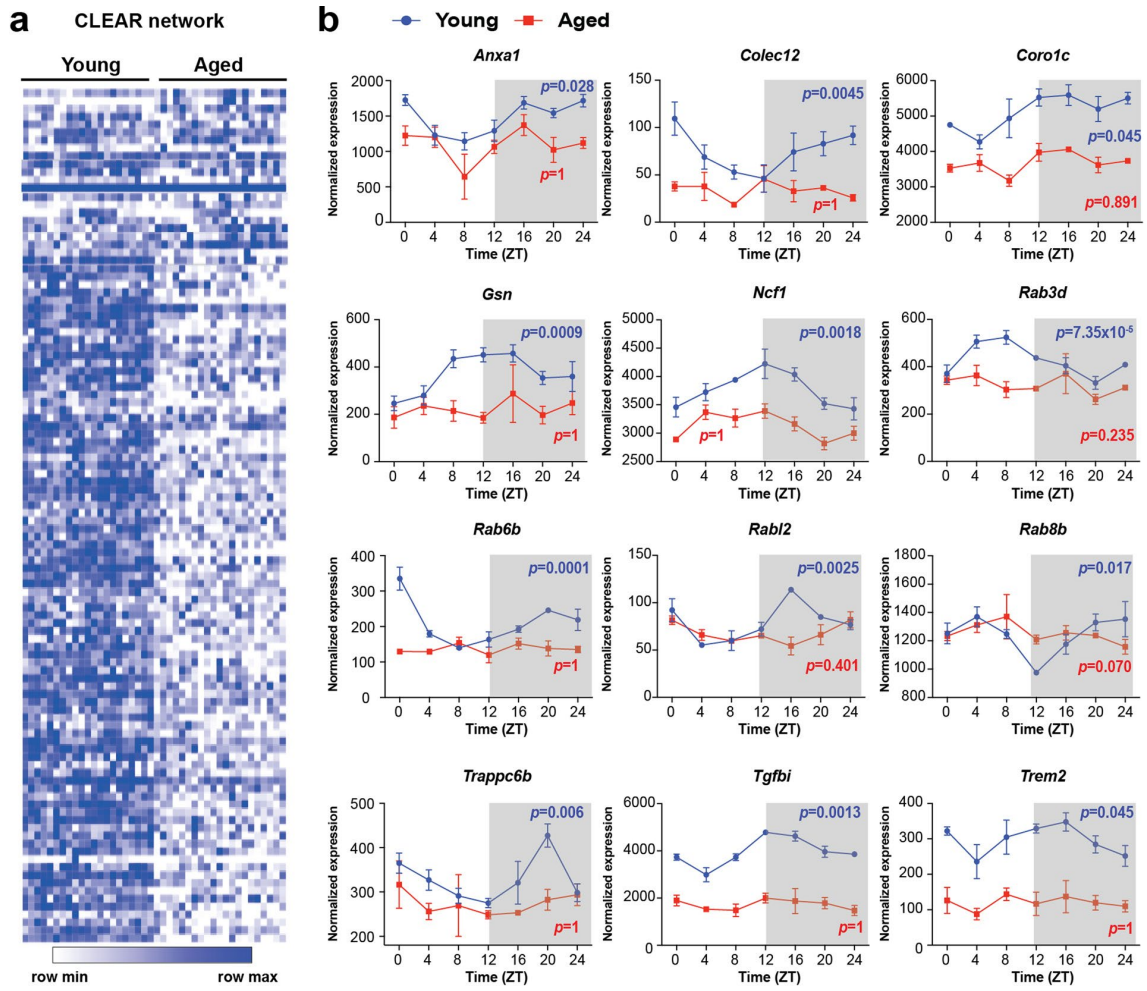

Extended Data Fig. 4 | Loss of circadian rhythmicity of phagocytosis gene expression in aged macrophages. a. Heatmap of normalized CLEAR network gene expression values of all time points for each age group shows a decrease in overall gene expression in aged as compared to young peritoneal macrophages. **b**. Circadian RNA-seq expression patterns of phagocytosis-related genes reveal loss of rhythmicity in aged peritoneal as compared to young macrophages. Data are mean ± s.e.m, n = 21 mice in each age group and n = 3 in each time group. Indicated p-values were calculated by JTK_CYCLE on normalized expression values.

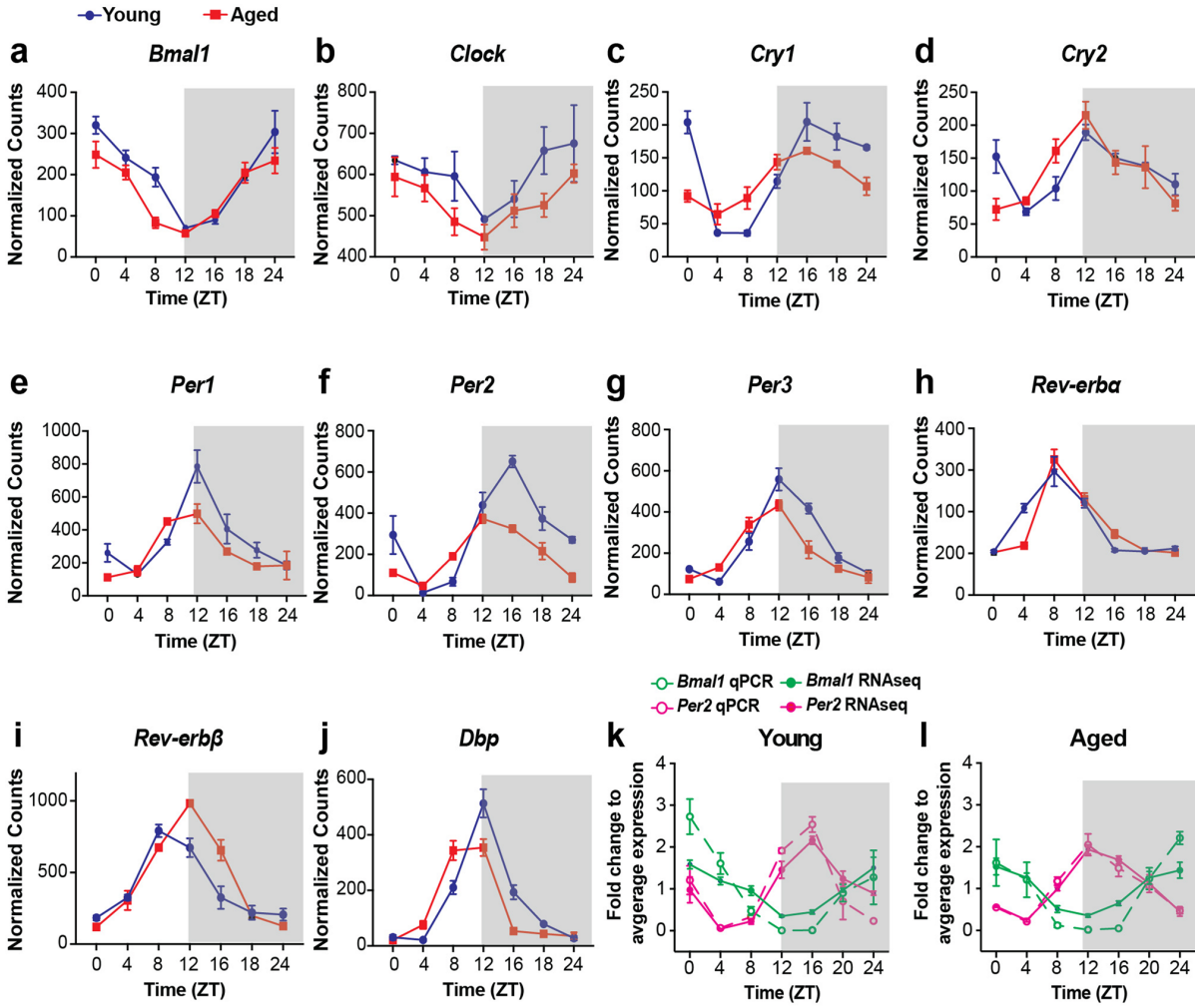

Extended Data Fig. 5 | The core circadian clock genes remain rhythmic in aged peritoneal macrophages. a-j, Individual representations of normalized circadian gene expression values measured by RNA-seq of the positive arm (a-b), negative arm (c-g) and supporting genes (h-j) of the core clock machinery. (k-l) qPCR validation of Bmal1 and Per2 expression in young and aged peritoneal macrophages. Data are mean ± s.e.m, n = 21 mice in each age group and n = 3 in each time group.

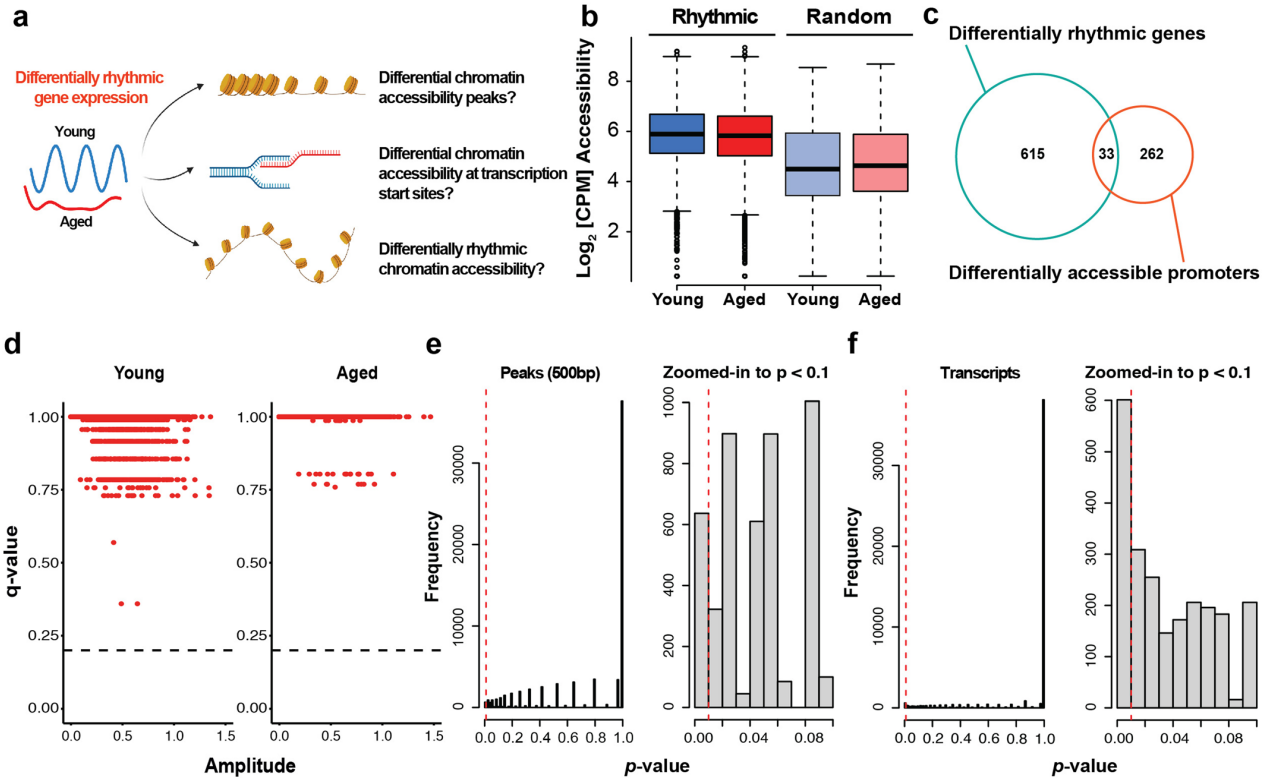

Extended Data Fig. 6 | Chromatin accessibility of young and aged macrophages is not rhythmic. a. Schematic of investigated possible explanations for differentially rhythmic gene expression by chromatin accessibility. **b**. Chromatin accessibility (as normalized and log2-transformed values) of promoter regions of differentially rhythmic genes between young and aged peritoneal macrophages. Note that rhythmically expressed genes have higher chromatin accessibility compared to an equal number of randomly selected control genes. n = 15-16 mice in each age group and n = 2-3 mice per 4 h time interval. Boxes extend from the 25th-75th percentiles, whiskers extend to 1.5 times the IQR, and the center line is the median. **c**. Venn diagrams of the numbers of differentially rhythmic genes between the two age groups (RNA-seq) and the numbers of differentially accessible promoter regions assessed by ATAC-seq. **d**, Scatterplots of amplitude and q-value for open chromatin peaks as assessed by JTK_CYCLE. No element shows $q < 0.2$ (indicated by dotted line). **e, f**, Distribution of unadjusted p-values for oscillations of open chromatin peaks (e) and transcripts (f) in young macrophages, zoomed-in to $p < 0.1$, JTK_CYCLE.

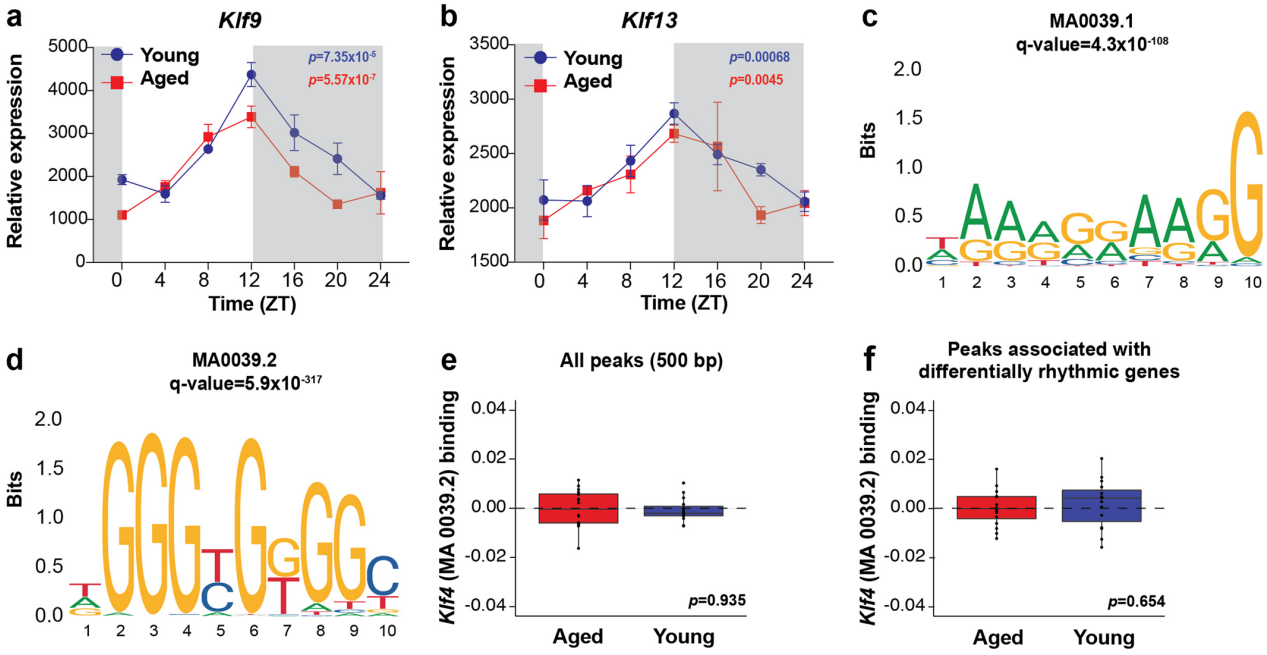

Extended Data Fig. 7 | Two distinct DNA binding motifs of KLF4. a, b. Circadian expression levels measured by RNA-seq of KLF family members Klf9 and Klf13. Data are mean ± s.e.m, n = 21 mice in each age group and n = 3 in each time group. p-values determined by JTK_CYCLE on normalized expression values. **c, d**. Depiction of the two known KLF4 binding motifs, MA0039.1 and MA0039.2. q-values from de novo motif discovery on a KLF4 ChIP-seq experiment from ENCODE (https://factorbook.org/experiment/ENCSR265WJC/motif). **e**. chromVAR30 deviations within all 500 bp peaks indicating KLF4 binding by estimating accessibility within peaks sharing the MA0039.2 motif or annotation. p = 0.935, two-sided Mann-Whitney U test. **f**. chromVAR30 deviations within peaks associated with differentially rhythmic genes indicating KLF4 binding by estimating accessibility within peaks sharing the MA0039.2 motif or annotation. p = 0.654, two-sided Mann-Whitney U test. (e, f) n = 15-16 mice in each age group and n = 2-3 mice per 4 h time interval. Boxes extend from the 25th-75th percentiles, whiskers extend to 1.5 times the IQR, and the center line is the median.

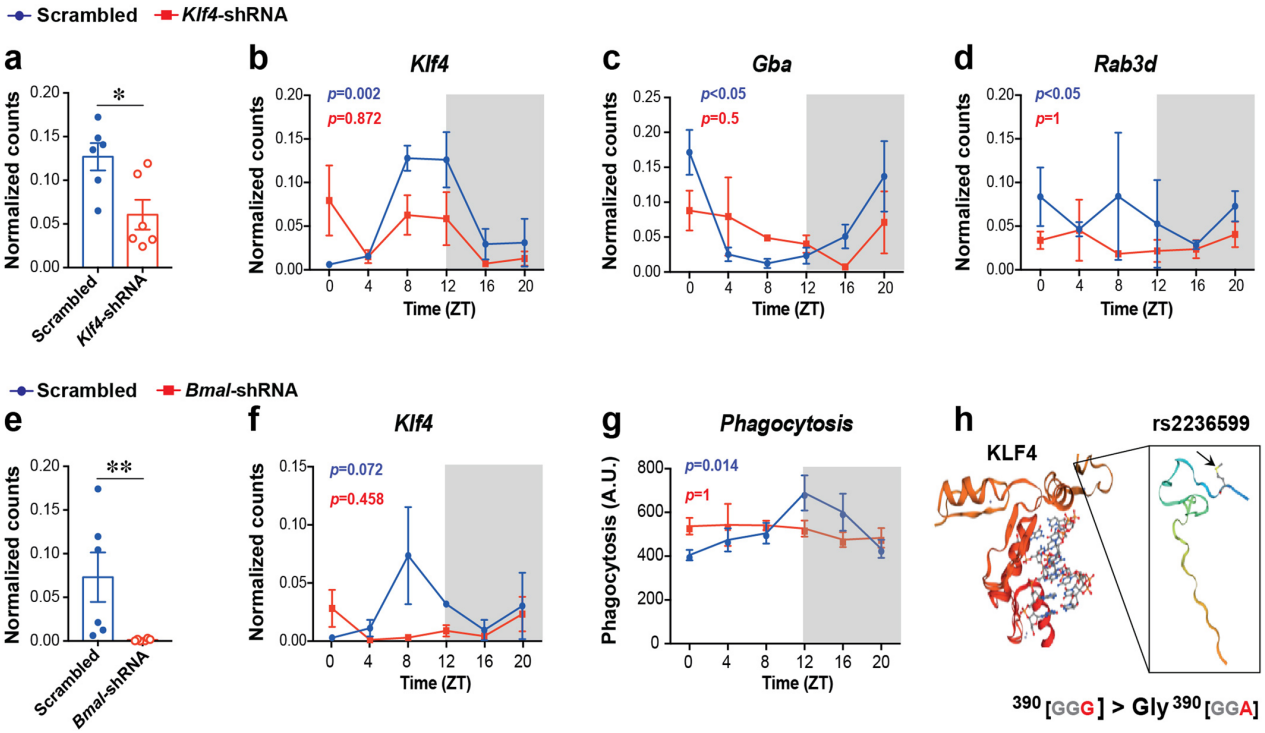

Extended Data Fig. 8 | Klf4 is controlled by Bmal1 and drives circadian rhythmicity of phagocytosis. a-d. Circadian RT-PCR expression patterns of Klf4 (a-b), and the phagocytosis-related genes Gba (c) and Rab3d (d) reveal loss of rhythmicity of phagocytosis genes in Klf4-shRNA lentiviral injected young mice as compared to scrambled vector controls. Data are mean ± s.e.m, n = 18 mice in each treatment group and n = 3 in each time group. Indicated p-values were calculated by JTK_CYCLE. **e-f**. RT-PCR expression of Bmal1 (e) and Circadian RT-PCR expression patterns of Klf4 in Bmal1-shRNA lentiviral injected young mice as compared to scrambled vector controls. Data are mean ± s.e.m, n = 18 mice in each treatment group and n = 3 in each time group. Indicated p-values were calculated by JTK_CYCLE. **g**. Phagocytosis of fluorescent E. coli particles by Bmal1-shRNA lentiviral and scrambled vector injected young mice. Data are mean ± s.e.m, n = 18 mice in each treatment group and n = 3 in each time group. Indicated p-values were calculated by JTK_CYCLE. **h**. Crystal structure of the zinc-finger domain of KLF4 in complex with DNA and rs2236599 synonymous mutation site predicted by SWISS-MODEL[57].

nature portfolio

Corresponding author(s): Katrin Andreasson

Last updated by author(s): Oct, 15 2021

Reporting Summary

Nature Portfolio wishes to improve the reproducibility of the work that we publish. This form provides structure for consistency and transparency in reporting. For further information on Nature Portfolio policies, see our Editorial Policies and the Editorial Policy Checklist.

Statistics

For all statistical analyses, confirm that the following items are present in the figure legend, table legend, main text, or Methods section.

n/a	Confirmed
☐	☒ The exact sample size (*n*) for each experimental group/condition, given as a discrete number and unit of measurement
☐	☒ A statement on whether measurements were taken from distinct samples or whether the same sample was measured repeatedly
☐	☒ The statistical test(s) used AND whether they are one- or two-sided *Only common tests should be described solely by name; describe more complex techniques in the Methods section.*
☐	☒ A description of all covariates tested
☐	☒ A description of any assumptions or corrections, such as tests of normality and adjustment for multiple comparisons
☐	☒ A full description of the statistical parameters including central tendency (e.g. means) or other basic estimates (e.g. regression coefficient) AND variation (e.g. standard deviation) or associated estimates of uncertainty (e.g. confidence intervals)
☐	☒ For null hypothesis testing, the test statistic (e.g. *F*, *t*, *r*) with confidence intervals, effect sizes, degrees of freedom and *P* value noted *Give P values as exact values whenever suitable.*
☒	☐ For Bayesian analysis, information on the choice of priors and Markov chain Monte Carlo settings
☐	☒ For hierarchical and complex designs, identification of the appropriate level for tests and full reporting of outcomes
☐	☒ Estimates of effect sizes (e.g. Cohen's *d*, Pearson's *r*), indicating how they were calculated

Our web collection on statistics for biologists contains articles on many of the points above.

Software and code

Policy information about availability of computer code

Data collection	QuantStudio6, FlowJo software, version 10.6.1.
Data analysis	Graphpad prism version 7, Microsoft Excel version 16.16.27, Trim Galore! version 0.6.4_dev, ChrAccR (https://greenleaflab.github.io/ChrAccR/articles/overview.html), Genrich (version 0.6, all default parameters), bedtools version 2.2.9.2, R, DESeq2 (version 1.28.1), chromVAR, JTK_cycle, RAIN, BooteJTK, MetaCycle

For manuscripts utilizing custom algorithms or software that are central to the research but not yet described in published literature, software must be made available to editors and reviewers. We strongly encourage code deposition in a community repository (e.g. GitHub). See the Nature Portfolio guidelines for submitting code & software for further information.

Data

Policy information about availability of data

All manuscripts must include a data availability statement. This statement should provide the following information, where applicable:

- Accession codes, unique identifiers, or web links for publicly available datasets
- A description of any restrictions on data availability
- For clinical datasets or third party data, please ensure that the statement adheres to our policy

Transcriptomics data: GSE128830: https://www.ncbi.nlm.nih.gov/geo/query/acc.cgi?acc=GSE128830
Token: ybqjocoontgtluf ; ATAC-seq data: https://purl.stanford.edu/rc797bt9574. The dataset used for the analyses in the UK Biobank have not been deposited in a public repository, but are available after approval of a reasonable application at https://www.ukbiobank.ac.ukl. For further information, please contact the corresponding author.

Field-specific reporting

Please select the one below that is the best fit for your research. If you are not sure, read the appropriate sections before making your selection.

☒ Life sciences ☐ Behavioural & social sciences ☐ Ecological, evolutionary & environmental sciences

For a reference copy of the document with all sections, see nature.com/documents/nr-reporting-summary-flat.pdf

Life sciences study design

All studies must disclose on these points even when the disclosure is negative.

Sample size	All in vivo experiment had at least N=3 in each group. The exact sample size for each experiment is reported in the Results, Methods and Figure legends sections. No statistical methods were used to pre-determine sample sizes but our sample sizes are similar to those reported in previous publications (Nguyen et al, 2013, Science 341: 1483-1488).
Data exclusions	No data were excluded from the manuscript
Replication	All the experiments in the manuscript were independently and successfully repeated at least 2 times unless otherwise stated
Randomization	All experiments were randomized and controlled for gender, weight and cage effects.
Blinding	In all experiments the researches were blinded

Reporting for specific materials, systems and methods

We require information from authors about some types of materials, experimental systems and methods used in many studies. Here, indicate whether each material, system or method listed is relevant to your study. If you are not sure if a list item applies to your research, read the appropriate section before selecting a response.

Materials & experimental systems

n/a	Involved in the study
☐	☒ Antibodies
☐	☒ Eukaryotic cell lines
☒	☐ Palaeontology and archaeology
☐	☒ Animals and other organisms
☒	☐ Human research participants
☐	☒ Clinical data
☒	☐ Dual use research of concern

Methods

n/a	Involved in the study
☒	☐ ChIP-seq
☐	☒ Flow cytometry
☒	☐ MRI-based neuroimaging

Antibodies

Antibodies used	Antibodies used against: CD45 (clone 30-F11, LOT: B247956, Cat# 103127), CD11b (clone M1/70, LOT: B253261, Cat# 101245), Ly6C (clone HK1.4, LOT: B268312, Cat# 128016), Ly6G (clone 1A8, LOT: B248965, Cat# 127623), CD115 (clone AF598, LOT: B265220, Cat# 135517), CD3 (clone 17A2, LOT: B304392, Cat# 100204), CD19 (clone 6D5, LOT: B251410, Cat# 115520) and F4/80 (clone BM8, LOT: B222447, Cat# 123128)
Validation	All the antibodies listed above were calibrated and validated for flow cytometry analysis including all compensation processes

Eukaryotic cell lines

Policy information about cell lines

Cell line source(s)	Jurkat, Clone E6-1, ATCC, TIB-152
Authentication	Cell line was not authenticated
Mycoplasma contamination	Cell line was tested negative for mycoplasma
Commonly misidentified lines (See ICLAC register)	N/A

Animals and other organisms

Policy information about studies involving animals; ARRIVE guidelines recommended for reporting animal research

Laboratory animals	Young (2-3 months old) JAX (C57BL/6J) and aged (20-22 months old) C57/BL6 male mice were used in the study. This study was conducted in accordance with NIH guidelines, and protocols were approved by the Institutional Animal Care and Use Committee at Stanford University. All mice were housed in an environment controlled, pathogen-free barrier facility on a 12 h light/dark cycle, temperature, and humidity, with food and water available ad libitum.
Wild animals	The study did not involve wild animals
Field-collected samples	The study did not involve samples collected from the field
Ethics oversight	This study was conducted in accordance with National Institutes of Health (NIH) guidelines; protocols were approved by the Institutional Animal Care and Use Committee at Stanford University.

Note that full information on the approval of the study protocol must also be provided in the manuscript.

Clinical data

Policy information about clinical studies

All manuscripts should comply with the ICMJE guidelines for publication of clinical research and a completed CONSORT checklist must be included with all submissions.

Clinical trial registration	The UKbiobank invited people aged 40 to 69 years to take part. All UK residents aged 40 to 69 years who were registered with the National Health Service and living up to 25 miles from 1 of the 22 study assessment centers were invited to participate. All participants gave informed consent for genotyping and data linkage to medical reports.
Study protocol	Genotyping of the KLF4 variant rs2236599 was conducted in a total of 488,377 subjects. Ongoing inpatient hospital records beginning in 1996 were used to identify diagnoses according to the International Classification of Diseases, Tenth Revision (ICD-10) codes.
Data collection	The presence of the following ICD10 codes was evaluated: Infection with E coli (A04) and Overall infections (A00-A99). The UK Biobank receives death notifications (age at death and primary ICD diagnosis that led to death) through linkage to national death registries. End of follow-up was defined as death or end of hospital inpatient data collection in June 2020. Specific causes of death included death by infection (A00-A99) and death by E.coli infection (A04). Detailed information about the study is available at the UKBB website (www.ukbiobank.ac.uk). The study has been approved by the UKB Access Committee (Project #59657).
Outcomes	The outcomes are depicted in Figure 4k-l

Flow Cytometry

Plots

Confirm that:

☒ The axis labels state the marker and fluorochrome used (e.g. CD4-FITC).

☒ The axis scales are clearly visible. Include numbers along axes only for bottom left plot of group (a 'group' is an analysis of identical markers).

☒ All plots are contour plots with outliers or pseudocolor plots.

☒ A numerical value for number of cells or percentage (with statistics) is provided.

Methodology

Sample preparation	Mouse peripheral blood, bone marrow and spleen samples were used in the study
Instrument	BD-LSR II cytometer
Software	FlowJo software, version 10.6.1
Cell population abundance	Cell populations sizes are reported in Extended Data Figure 1. Purity was validated using the appropriate single stained and isotype controls
Gating strategy	Gating strategy is reported in Extended Data Figure 1. The following controls were used: unstained cells, single-stained cells and dead cells. The cells were gated using forward and side scatter, as well as live/dead staining using DAPI (ThermoFisher Scientific).

☒ Tick this box to confirm that a figure exemplifying the gating strategy is provided in the Supplementary Information.